Geoscience Frontiers 16 (2025) 102172

Contents lists available at ScienceDirect

Geoscience Frontiers

journal homepage: www.elsevier.com/locate/gsf

Research Paper

Crustal contamination and insights into diachronous changes toward modern tectonics: evidence from Hf-Nd-O-Pb isotope of sanukitoids from the Amazonian craton

Aline Costa do Nascimento [a,b,*], Davis Carvalho de Oliveira [a,b], Esa Heilimo [c], Marco Antonio Galarza [a,d], Eleilson Oliveira Gabriel [a,b], Martin Whitehouse [e], Matti Kurhila [f], Cláudio Nery Lamarão [a,b,g]

[a] Postgraduate Program in Geology and Geochemistry (GPGG), Institute of Geosciences (IG), University Federal do Pará (UFPA), Box 1611, CEP 66075-100, Belém, Pará, Brazil
[b] Group of Research on Granitoids Petrology (GPPG), IG, UFPA, Brazil
[c] Department of Geography and Geology, University of Turku, Finland
[d] Laboratory of Isotopic Geology (Pará-Iso), IG, UFPA, Belém, PA, Brazil
[e] Swedish Museum of Natural History, Box 50007, SE-104 05 Stockholm, Sweden
[f] Geological Survey of Finland (GTK), P.O. Box 96, FI-02151 Espoo, Finland
[g] Laboratório de Microanálises (LAMICRO-IG-UFPA), Brazil

ARTICLE INFO

Article history:
Received 26 March 2025
Revised 20 August 2025
Accepted 29 September 2025

Keywords:
Sanukitoids
Isotope geochemistry
Crustal evolution
Subduction
Mesoarchean

ABSTRACT

Archean sanukitoids provide crucial insights into crust-mantle interactions during the early Earth's geodynamic evolution. However, the role of crustal contamination in their genesis remains uncertain. Sanukitoids identified in the Sapucaia subdomain of the southern Carajás Province are represented by two plutons Água Limpa and Água Azul, collectively referred to as the Água Limpa sanukitoid suite. These plutons are compositionally similar to low-Ti sanukitoids (< 0.63 % TiO_2) and their zircon isotopic data record a short period of magmatic activity around ca. 2.87 Ga. Sanukitoids zircons reveal $\varepsilon_{Hf}(t)$ values ranging from –3.31 to + 2.14, Hf and Nd model ages between 2.91 Ga and 3.28 Ga, whole-rock $\varepsilon_{Nd}(t)$ values from –1.64 to + 1.76, and $\delta^{18}O$ values ranging from 5.0 ‰ to 7.6 ‰. The Pb isotopic compositions in K-feldspar (μ > 10) suggests a Mesoarchean mantle source affected by slight crustal contribution and/or contamination. Result of geochemical modelling indicates that the sanukitoids were formed by ~ 15 % partial melting of mantle peridotite previously enriched by ~ 30 % of slab-derived melts, with orthopyroxene, garnet, clinopyroxene, phlogopite, and magnetite as residual phases. The integration of our data with previously published results leads us to suggest that modern-style plate tectonics may have initiated along the northern Carajás Province during the Mesoarchean, while the Rio Maria domain to the south remained dominated by mantle plume-driven crustal growth and vertical tectonics.

1. Introduction

Archean continental evolution is characterized by recurrent events of juvenile crustal growth and reworking, with varying contributions from mantle input (Laurent et al., 2014). Models explaining Archean crustal growth range from plume-driven mechanisms (e.g., Bédard, 2018) to processes akin to modern plate tectonics (e.g., Cawood et al., 2018). While there is significant debate about when plate tectonics began and its extension on early Earth (Palin et al., 2020), there is consensus that the transition between these mechanisms is witnessed by specific rocks, generally referred as late Archean sanukitoids (Martin et al., 2009). Sanukitoids play a significant role in elucidating uppermost mantle processes and the recycling of crustal materials within Archean cratons (Heilimo et al., 2013; Jiang et al., 2016; Fu et al., 2018; Sun et al., 2019, 2020, 2023; Silva et al., 2023). These rocks are interpreted to represent the earliest signs of interaction between felsic melts and a metasomatized mantle, potentially linked to an enriched mantle wedge (Martin et al., 2005). However, such signatures can also result from alternative crust-mantle dynamics not necessarily related to modern-style plate tectonics, such as litho-

* Corresponding author.
E-mail addresses: aline.nascimento@ig.ufpa.br (A.C. do Nascimento), davis@ufpa.br (D.C. de Oliveira), esa.heilimo@utu.fi (E. Heilimo), antogt@ufpa.br (M.A. Galarza), eleilson.gabrielufpa@gmail.com (E.O. Gabriel), Martin.Whitehouse@nrm.se (M. Whitehouse), matti.kurhila@gtk.fi (M. Kurhila), lamarao@ufpa.br (C.N. Lamarão).

https://doi.org/10.1016/j.gsf.2025.102172

spheric dripping (Nebel et al., 2018; Smithies et al., 2021) or lower crustal delamination (Johnson et al., 2014; Hu et al., 2019).

The term sanukitoid describes high-Mg plutonic granitoids with elevated Mg numbers (45 – 65), enriched in Ni (> 100 ppm), Cr (> 200 ppm), large-ion lithophile elements (Ba + Sr > 1400 ppm) (Heilimo et al., 2010). The oldest sanukitoids have been identified in the Pilbara Craton, Western Australia (2.95 Ga; Smithies and Champion, 2000) and the Amazonian Craton, Carajás Province (2.92 Ga and 2.89 – 2.87 Ga; Oliveira et al., 2011; Silva et al., 2023; Nascimento et al., 2024), although most of them are formed around 2.70 Ga (Heilimo et al., 2013). They are commonly associated with shear zones or tectonic boundaries, intruding basement rocks in Archean granite-greenstone terrains as late- to post-kinematic intrusions (Moyen et al., 2003). Petrogenetic models and experimental studies suggest that sanukitoids result from interactions between mantle peridotite and components enriched in incompatible trace elements, either through interaction with TTG melts formed by slab melting or with melts derived from subducted sedimentary rocks, both ultimately sourced from reworked ancient crust (Stern and Hanson, 1991; Stevenson et al., 1999; Rapp et al., 2010).

Mantle upwelling and heat conduction from the asthenosphere to the lithosphere play crucial role in crust-mantle interaction and the formation of distinct geochemical reservoirs (Laurent et al., 2020). Such recycling systems have been active since 3.85 Ga, as evidenced in early Archean rocks, and are better understood for post-Archean terranes (Schneider et al., 2018). U-Pb-Hf isotopes in zircon and Nd isotopes in whole rock have been widely used to investigate crust formation processes and their timing during the Early to Mid-Archean, although interpretations remain debated (Laurent et al., 2020). Some contradictions can be better constrained by the additional application of stable oxygen isotopes ($\delta^{18}O$) in zircon and Pb isotopes in K-feldspar, as these isotopic systems serve as magma source tracers, providing insights into the incorporation of subducted sediments and magma genesis under varying surface and magmatic conditions (e.g, Kemp et al., 2010; Vervoort and Kemp, 2016; Halla, 2018). Understanding these interactions is essential for unraveling Earth's recycling engine and its role in magmatic evolution (Vervoort and Kemp, 2016).

To investigate crustal recycling and isotopic signatures of Mesoarchean sanukitoids, we obtained Sm-Nd data in whole-rock, Lu-Hf and $\delta^{18}O$ isotope in zircon, and Pb isotopic compositions in K-feldspar from the Água Limpa and Água Azul plutons, Carajás Province. Hf-O-Nd-Pb isotopic systematics help distinguish between well-mixed mantle sources, ancient mafic components or recycled sedimentary materials (Halla, 2005, 2018; Heilimo et al., 2013). By targeting igneous zircon domains previously dated by U-Pb SHRIMP methodology (Nascimento et al., 2024), we provide a detailed temporal view of source evolution, magmatic processes and mantle-crust interactions, either through mantle contamination via subduction or direct crustal assimilation. This study elucidates: (1) the petrogenesis of the Água Limpa sanukitoid suite, (2) isotopic constraints (Hf-O-Nd-Pb) on crust-mantle interactions, and (3) geodynamic mechanisms underlying crustal growth in the Sapucaia subdomain. These insights from the Carajás Province contribute to understanding the diachronous transition to modern tectonic processes.

2. Geological background

The Amazonian Craton is situated north of the South American platform and represents one of the most well-preserved cratons worldwide (Fig. 1a; Almeida et al., 1981). This continental block formed through amalgamation of Paleoproterozoic and Mesoproterozoic belts, achieved stability by the end of the Mesoproterozoic, with minimal impact from the surrounding Brasiliano-Pan African orogens (Cordani et al., 2000). The Carajás Province represents the Archean nucleus of the Amazonian Craton and consists of two main tectonic domains separated by E–W regional shear zones: the Rio Maria Domain to the south and the Carajás Domain to the north (Fig. 1b). These two terranes evolved independently before amalgamating during the Mesoarchean (Cordani et al., 2000; Vasquez and Rosa-Costa, 2008).

The Mesoarchean Rio Maria Domain (3.07 – 2.93 Ga) is a typical low-grade granite-greenstone terrane featuring large (45 – 35 km diameter) dome-like structures flanked by curvilinear belts of metavolcanic and metasedimentary rocks (the Andorinhas greenstone belts with ages of 3.02 – 2.97 Ga; Vasquez and Rosa-Costa, 2008). The basement also includes TTG suites 2.98 – 2.92 Ga in age (Almeida et al., 2011, 2013). Granitic complexes are represented mostly by sanukitoids from the Rio Maria Suite, with minor occurrence of stocks of potassic and hybrid granites that are 2.88 – 2.87 Ga in age, displaying a regional fabric with a NW–SE to E–W orientation (Oliveira et al., 2010; Santos and Oliveira, 2016). Archean sedimentary sequences partly overlie these lithologies (Vasquez and Rosa-Costa, 2008). In opposite, the Meso- to Neoarchean Carajás Domain (3.07 – 2.70 Ga) is a high-grade gneiss terrane interpreted to be dominated by vertical tectonics. It is subdivided into three subdomains: the Sapucaia Subdomain, Canaã dos Carajás Subdomain, and Carajás Basin (Fig. 1c; Dall'Agnol et al., 2013). Its basement assemblage underwent regional deformation in the Mesoarchean (3.02 – 2.85 Ga) related to the collision of the Carajás and Rio Maria Domains (Marangoanha et al., 2020). During this event, WNW–ESE-trending ductile sinistral strike-slip and thrust shear zones with SW to NE transport developed (Pinheiro and Holdsworth, 2000). However, the rocks of the Rio Maria Domain were weakly affected by this event (Almeida et al., 2011). The Canaã dos Carajás Subdomain comprises the basement of the basin and represents an imbricated and anastomosing structure (oriented E–W) (Pinheiro and Holdsworth, 2000). This terrane differs from the Rio Maria Domain in terms of the scarcity of TTGs, the dominance of biotite granites and the presence of migmatites, granulites and charnockites (Feio et al., 2013; Felix et al., 2020; Marangoanha et al., 2020). The Sapucaia Subdomain, hosting the study area, is formed by migmatized gneisses and greenstone belt featuring deformational episodes of varying intensity (Nascimento et al., 2024). These rocks are intruded by sanukitoids of the Água Limpa Suite, potassic and hybrid granites from Xinguara and Nova Canadá units, respectively, and diverse mafic rocks including the Surucucu amphibolite (Oliveira et al., 2023; Fig. 1c). Neoarchean magmatism is represented mostly by the Vila Jussara granites (Silva et al., 2020). The Carajás Basin consists of metavolcanosedimentary sequences (> 2.76 Ga) intruded by mafic – ultramafic rocks and subalkaline granites (Vasquez and Rosa-Costa, 2008). At 1.88 Ga, the province experienced voluminous anorogenic granitic plutonism (Dall'Agnol and Oliveira, 2007).

3. Geology, age, structural aspects and petrography

The Água Limpa suite comprise two plutons of sanukitoid affinity, known as Água Limpa and Água Azul (Fig. 2). The former covers an area of 126 km^2 and is located to the north of the studied area, while the latter spans 62 km^2 to the south (Fig. 3a; Gabriel and Oliveira, 2014). These granitoids intrude the Sapucaia greenstone belt and the gneiss migmatized basement of the Sapucaia subdomain, dated at 3.02 – 2.95 Ga (Fig. 3b; Nascimento et al., 2023). The sanukitoids exhibit flattened amphibolite and metabasalt xenoliths at outcrop (Fig. 3c). They are intruded by the Boa Sorte potassic granite (Fig. 3d) and Nova Canadá hybrid leucogranodiorite (Fig. 3e), both dated at 2.87 Ga (Leite-Santos and Oliveira, 2016).

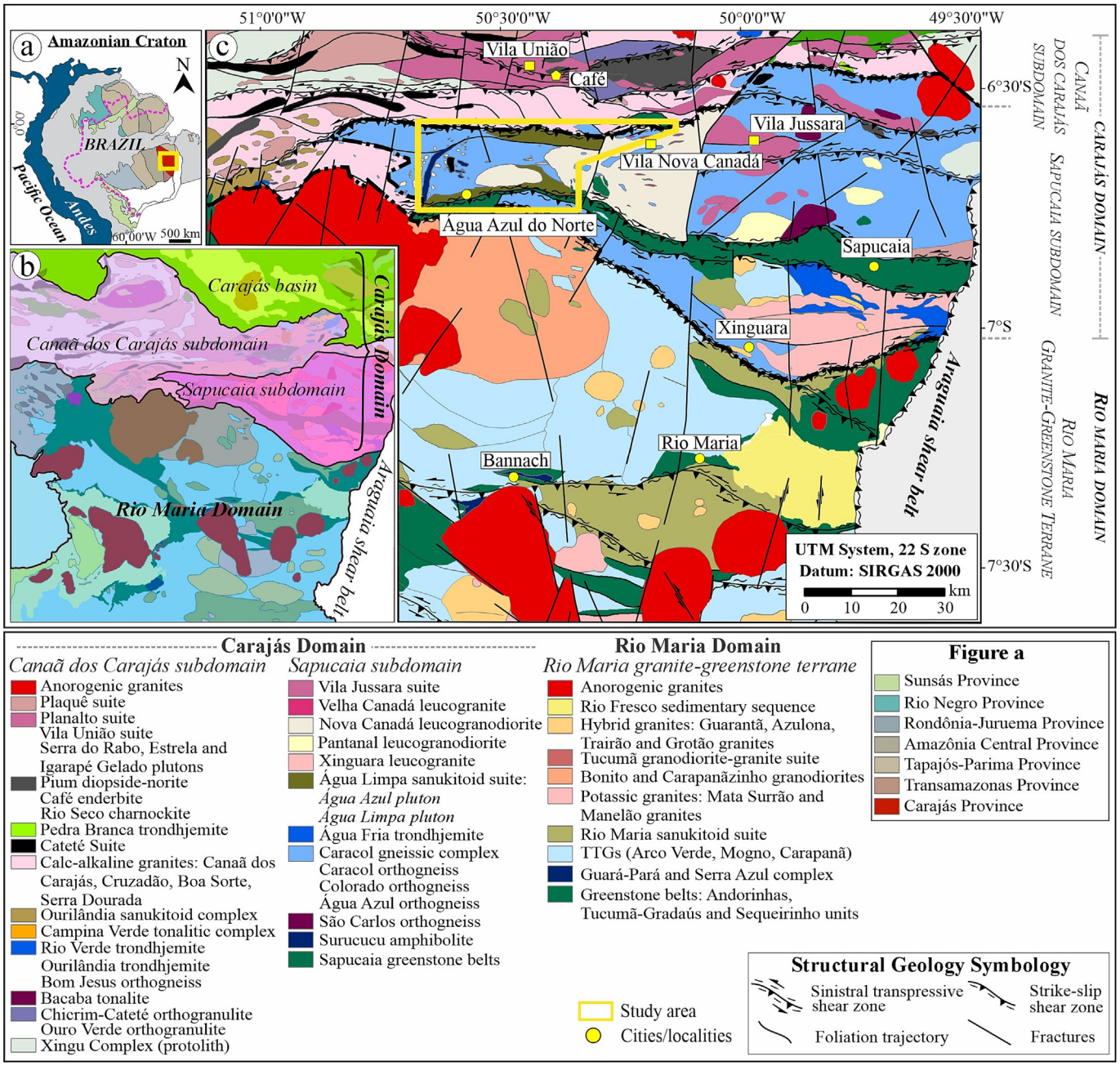

Fig. 1. Regional context of the Carajás Province: (a) location of the Amazonian Craton and Carajás Province (highlighted in a yellow square) on the South American platform (Almeida et al., 1981), with geochronological provinces based on Tassinari and Macambira (2004) and tectonic boundaries sourced from Santos (2003); (b) updated subdivision of the lithotectonic terranes (Dall'Agnol et al., 2013; Oliveira et al., 2023); (c) geological map of the Carajás Province, illustrating the detailed study area (Nascimento et al., 2023, 2024).

Additionally, potassic and subalkaline granites, from the Velha Canadá leucogranite and the Vila Jussara suite, respectively, with ages from 2.73 Ga to 2.74 Ga, crosscut the sanukitoid plutons (Silva et al., 2020). Zircon Pb–Pb ages of 2.88 Ga and 2.87 Ga were obtained for the Água Azul and Água Limpa plutons, respectively, by Gabriel et al. (2010) and Sousa et al. (2010). Recently, new U-Pb SHRIMP dating yielded ages of 2.87 Ga for the Água Limpa pluton and 2.87 Ga for the Água Azul pluton, corroborating previous dating results (Nascimento et al., 2024).

These sanukitoid rocks occur along the borders of the E–W-trending transpressive shear zones, acting as a boundary between the Carajás and Rio Maria domains (Fig. 1). They exhibit heterogeneous deformation, with mylonitic foliation trending E–W to WNW–ESE and displaying moderate to steep dips (40° – 89°) toward the south (Fig. 2; Nascimento et al., 2024). Asymmetries, such as C/S fabric, stair-stepping rotated porphyroclasts and "s" folds, indicate a sinistral sense of shear in this zone. Mineral stretching lineation also show steep to subvertical plunges (60° – 85°) toward both the N and S, suggesting transpression. Fractures with N–S, NW–SE and NE–SW orientations crosscut the studied sanukitoids, coinciding with those observed in the Neoarchean mafic dikes (Nascimento et al., 2024).

The dominant lithology in both sanukitoid plutons is porphyritic granodiorite, with minor occurrences of tonalites and monzogranites (Fig. 3f–l; Gabriel and Oliveira, 2014). Foliation is characterized by the preferred orientation of mafic minerals and,

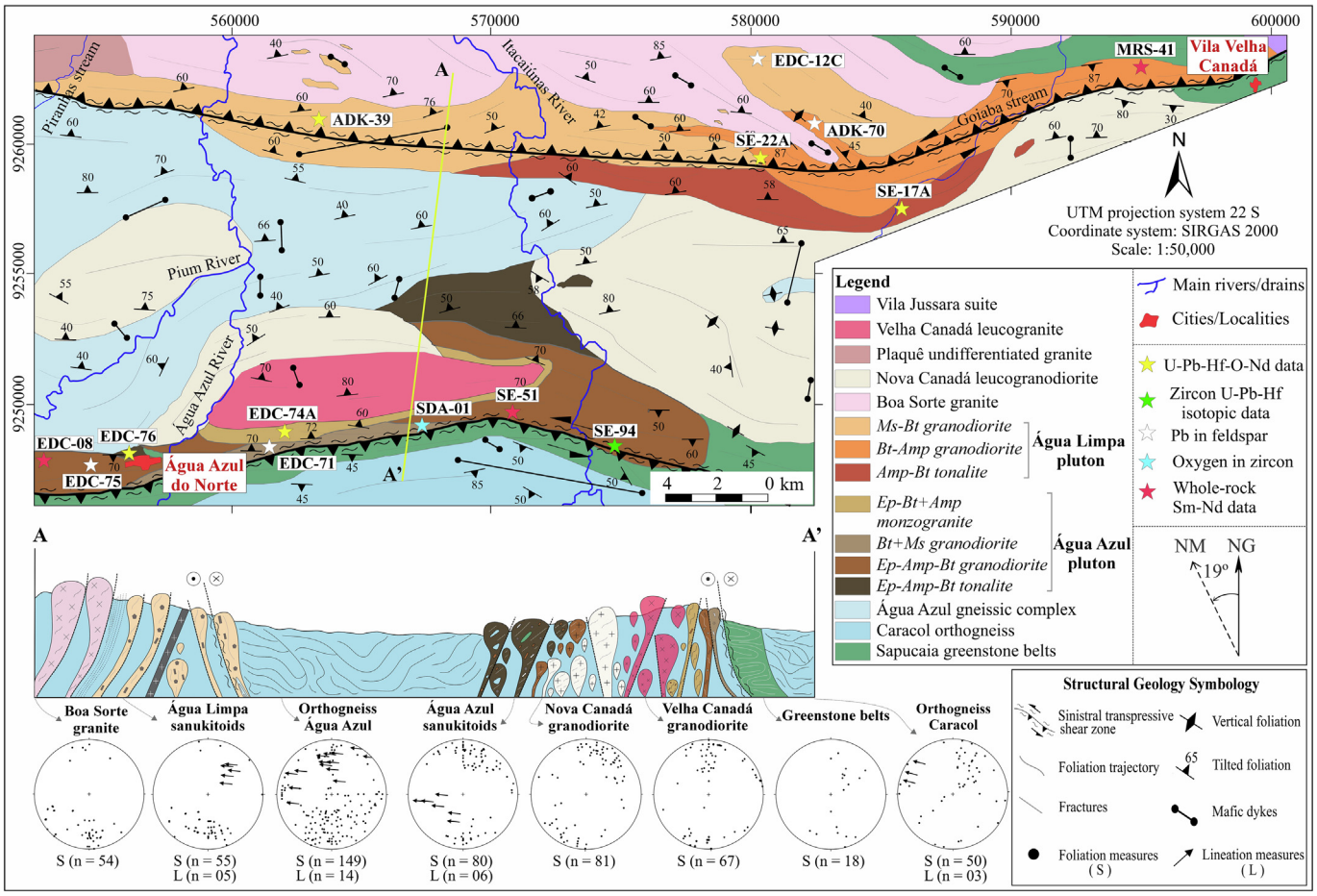

Fig. 2. Geological map of the Água Azul do Norte area, showing the locations of samples analyzed using Hf-O-Pb-Nd isotopes. The map illustrates the petrographic facies identified in the Água Limpa sanukitoid suite (Gabriel and Oliveira, 2014). A schematic profile (A-A') provides interpretations of the deep structure, while equal-area stereographic projections (Schmidt-Lambert) display the measured foliations and lineations (Nascimento et al., 2024). The coordinate system used for latitude and longitude is SIRGAS 2000. Abbreviations: NM = Magnetic North; NG = Geographic North; L = lineation; S = foliation; Ms = muscovite; Bt = biotite; Amp = amphibole; Ep = epidote; U = uranium; Pb = lead; O = oxygen; Hf = hafnium; Nd = neodymium; Sm = samarium.

locally, by mafic enclaves that align with the E-W foliation trend (Fig. 3j). These rocks are dark gray to dark green in color, exhibiting porphyritic or medium- to coarse-grained textures. The phenocrysts consist of microcline and orthoclase (0.5 – 3.0 cm in size) with subordinate plagioclase, set within a medium- to fine-grained matrix (< 3 mm) enriched in mafic minerals (Fig. 3m; M = 29 – 21 wt.%; Gabriel and Oliveira, 2014). The matrix is composed primarily of orthoclase and plagioclase (49.5 – 32.9 wt.%), quartz (29.2 – 19.7 wt.%), and microcline (~11 – 1 wt.%), with biotite, amphibole, and epidote are the main varietal phases (~ 27 – 10 wt.%). Accessory minerals include zircon, apatite, magnetite, ilmenite, titanite, muscovite, and allanite (5 wt.%). Secondary phases such as chlorite, muscovite, hematite, goethite, pyrite, sericite, carbonate, scapolite, titanite, and epidote are also present. All petrographic varieties across both sanukitoid plutons exhibit similar mineral assemblages (Fig. 3n–p; Gabriel and Oliveira, 2014; Nascimento et al., 2024).

Intense and widespread deformation is evident in these sanukitoid rocks, where the original porphyritic texture has been overprinted by a mylonitic texture, showing a gradual transition between the two (Fig. 3q). The heterogeneous strain observed in sanukitoids is reflected in the feldspar phenocrystals, which vary from tabular (euhedral) forms to elliptical porphyroclast (Nascimento et al., 2024). In the high-strain domains, the granitoids exhibit foliation defined by the preferred orientation of clustered mafic aggregates, feldspar porphyroclasts, core-and-mantle structures, and stretched polycrystalline aggregates within a bulging (BLG) and subgrain rotation (SGR) recrystallized matrix. Evidence of grain boundary migration recrystallization (GBAR) is also locally present. The clustered aggregates consist of amphibole porphyroclasts, sometimes displaying ocellar fish-like format, bordered by biotite and minor quartz and epidote. The matrix primarily comprises a medium- to fine-grained polygonal granoblastic fabric of K-feldspar, plagioclase, quartz, biotite, muscovite, minor epidote and amphibole in stretched aggregates surrounding the porphyroclasts, along with quartz ribbons (Fig. 3q; Nascimento et al., 2024).

4. Whole-rock geochemistry

In the Na_2O/K_2O vs. 2A/CNK vs. 2FMBS diagram (Fig. 4a; Laurent et al., 2014), the sanukitoids of the Água Limpa suite plot within the global field typical of Archean sanukitoids *latu sensu*, characterized by high Fe (1.3 – 6.7 wt.%), Mg (2.5 – 4.8 wt.%), K (2.1 – 4.3 wt.%), Ba (519 – 1966 ppm), Sr (477 – 912 ppm) and P (262 – 1047 ppm) contents (Gabriel and Oliveira, 2014). They exhibit moderate $(Ce/Yb)_N$ values ranging from 14.0 to 30.6, except for the muscovite-bearing sanukitoids from the Água Limpa pluton, which show significantly higher values (44.2 – 95.6) (Fig. 4b). These rocks are calc-alkaline to calcic with metaluminous to slightly peraluminous nature (0.8 < A/CNK < 0.9) (Figs. 4c, d).

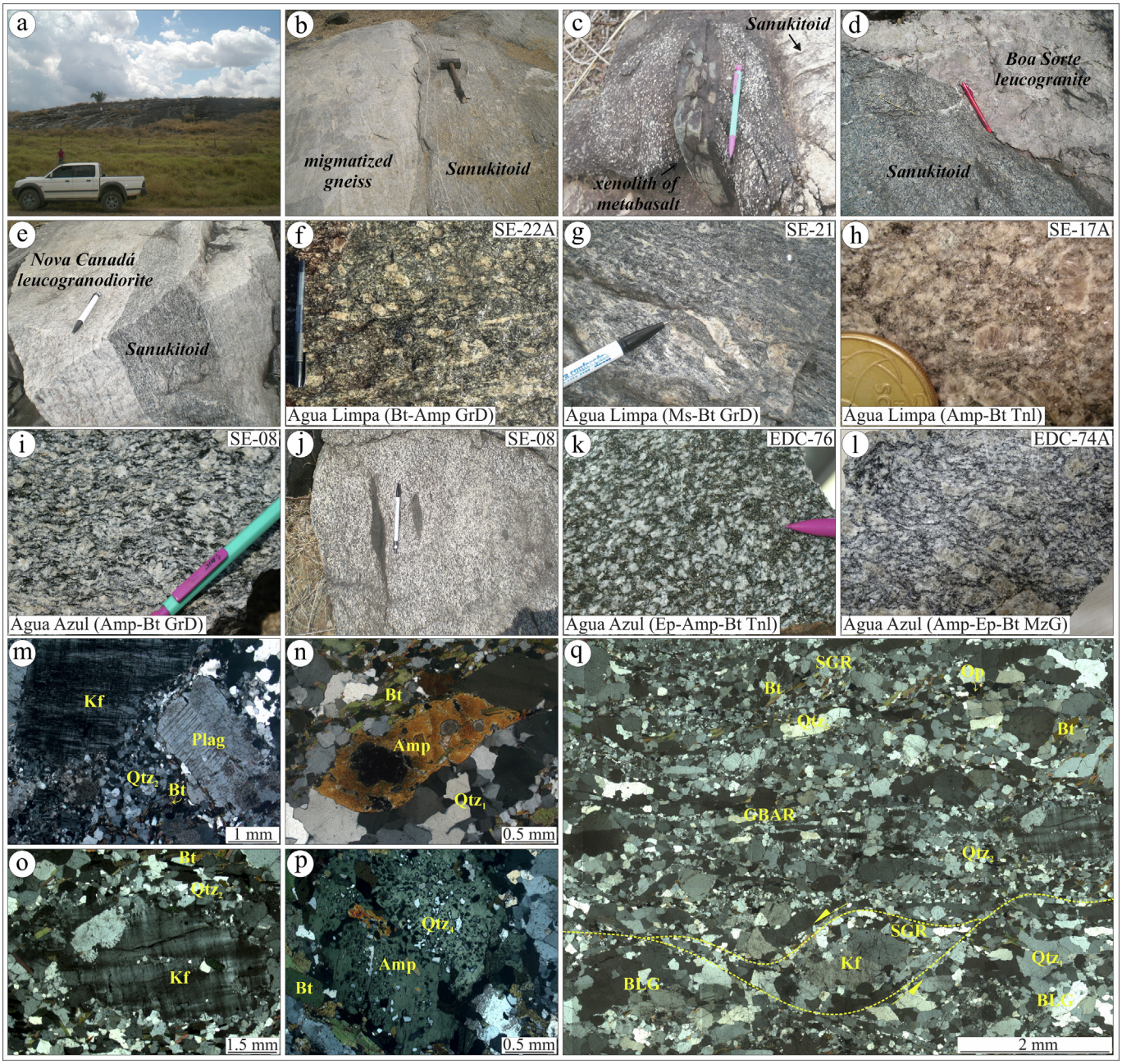

Fig. 3. Field relationships and microstructural aspects of the Água Limpa sanukitoid suite. (a) An outcrop of granodiorite from the type area; (b-d) granodiorite and tonalite facies from the Água Limpa pluton, both characterized by porphyritic textures, displaying deformed alkali feldspar phenocrysts; (e-h) granodiorite, tonalite, and monzogranite facies from the Água Azul pluton, showing a porphyritic texture with a crenulated aspect and the presence of rare mafic enclaves oriented according to the rock foliation trend; (i-l) field relationship characterized by a xenolith of metabasalt from the Sapucaia greenstone belt enclosed in the studied sanukitoid, contact with migmatized gneiss, potassic and hybrid granites (Boa Sorte and Nova Canadá, respectively); (m-p) microstructural features with feldspar phenocrysts bordered by a recrystallized quartz-feldspathic matrix and amphibole phenocrysts with an ocellar (fish-type) format. It mineral shows disequilibrium texture; (q) general overview of the microstructural aspect of granodioritic facies of sanukitoids in high-strain domain. Abbreviations: Bt = biotite; Amp = amphibole; Ms = muscovite; Ep = epidote; Kf = alkali feldspar; Plag = plagioclase; Qtz = quartz; GrD = granodiorite; Tnl = tonalite; MzG = monzogranite; BLG = bulding; SGR = subgrain rotation; GBAR = grain-boundary area rotation.

According to the FeO_T/ (FeO_T + MgO) vs. SiO_2 diagram (Fig. 4e; Frost et al., 2001), samples from both sanukitoid plutons resemble high magnesium granitoids and are classified as low Ti sanukitoids (Fig. 4f; Martin et al., 2009). They display geochemical signatures indicative of sanukitoids originating from a high-K mafic source, reflective of an enriched mantle (Fig. 4g; Laurent et al., 2014), with a contribution from crustal mixing source (Fig. 4h). The muscovite-bearing granodiorite variety from the Água Limpa pluton represents a more evolved member associated with a garnet-controlled source, whereas the amphibole-bearing granodiorite from the Água Azul pluton represents a less evolved member associated with a nongarnet-controlled source (Fig. 4i). Further geochemical discussion can be found in Gabriel and Oliveira (2014) and Nascimento et al. (2024).

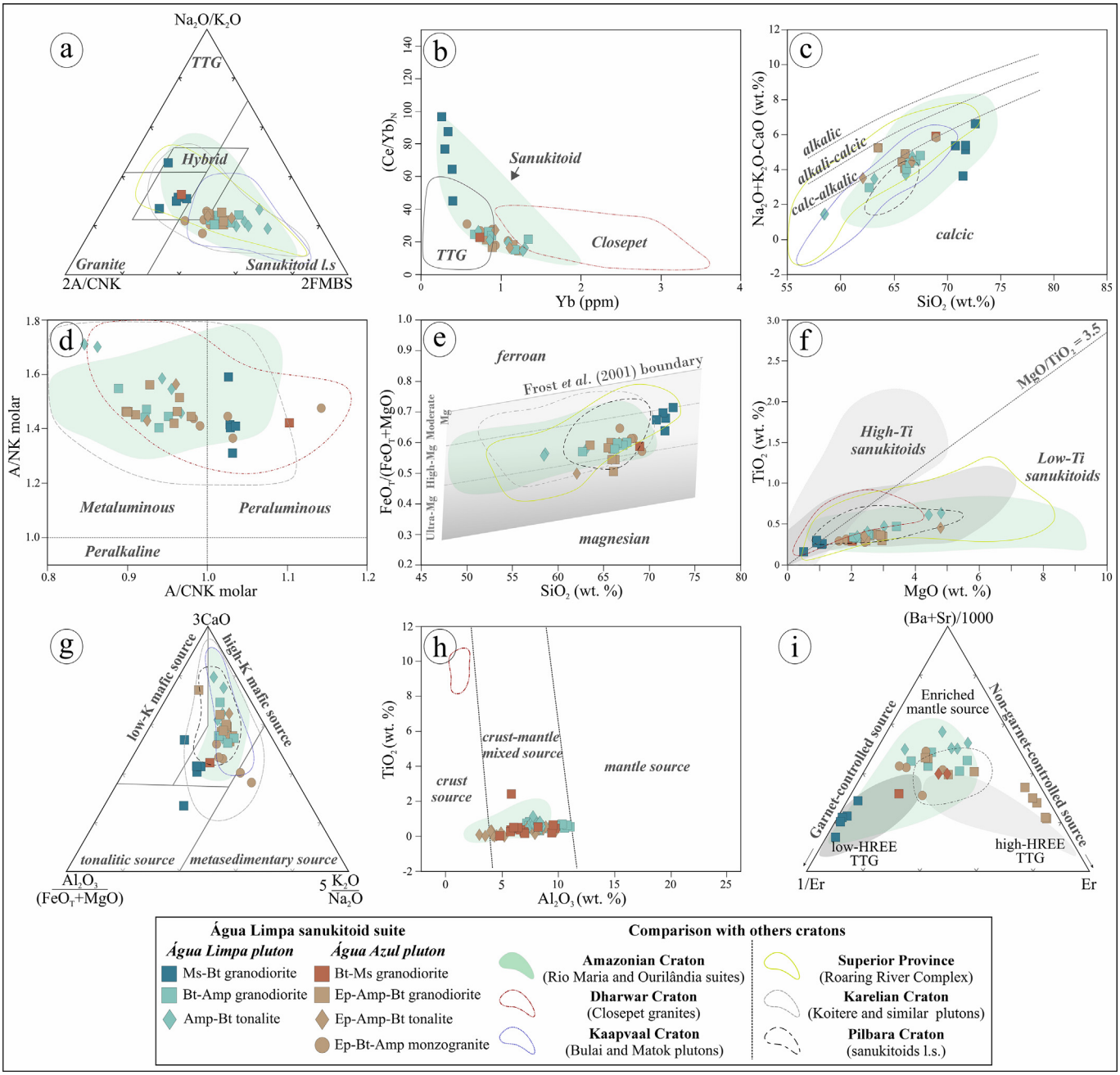

Fig. 4. Geochemical classification diagrams for magmatic rocks and series. (a) Ternary diagram for late Archean granitoids (Laurent et al., 2014), with axes defined as Na_2O/K_2O (wt.%); 2A/CNK = 2 × [Al_2O_3 / (CaO + Na_2O + K_2O)] molar; FMBS = 2 × (FeO_T + MgO, wt.%) × (Sr + Ba, ppm). (b) Binary discriminant diagram, $(Ce/Yb)_N$ vs. Yb (ppm). (c) Na_2O + K_2O – CaO vs. SiO_2 diagram (Frost et al., 2001). (d) A/NK [Al_2O_3 / (Na_2O + K_2O), molar] vs. A/CNK [Al_2O_3 / (CaO + Na_2O + K_2O), molar]. (e) FeO_T/ (FeO_T + MgO) vs. SiO_2 (wt.%) (Frost et al., 2001; Terentiev and Santosh, 2018). (f) TiO_2 (wt.%) vs. MgO (wt.%), with fields of high- and low-TiO_2 sanukitoids from Martin et al. (2009) shaded in light and dark gray, respectively. (g) Source discriminant diagram for Archean granitoids (Laurent et al., 2014). (h) Discriminant diagram of TiO_2 (wt.%) vs. Al_2O_3 (wt.%) based on mineral chemistry in amphibole (Nascimento et al., 2023). (i) Discriminant diagram of garnet-controlled (pole 1/Er) and nongarnet-controlled (pole Er) sources; the third pole, (Ba + Sr)/1000, represents an enriched mantle source (Heilimo et al., 2010).

5. Significance of the present study

While previous studies have provided robust petrographic, structural, geochemical, and geochronological frameworks, critical gaps remain in understanding the isotopic characteristics of the magma source, the role of crust–mantle interactions, and the geodynamic setting of magma emplacement. This study pioneers the application of Lu-Hf isotopes in zircon (via LA-ICP-MS) and oxygen isotopes ($\delta^{18}O$) in zircon (via SIMS) in sanukitoids from the Carajás Province. These data enable the discrimination between juvenile mantle-derived magmas and reworked crustal components, providing new constraints on source heterogeneity. In addition, the integration of whole-rock Sm-Nd isotopes, Pb isotopes in K-feldspar (via LA-ICP-MS), and geochemical modeling allows for detailed quantification of partial melting processes, crustal assimilation, and mantle metasomatism. This multi-isotopic approach addresses ongoing controversies about the extent of crustal versus mantle contributions to Archean sanukitoid magmatism of the Água Limpa suite. By combining these innovative isotopic tools with detailed petrological and tectonic analysis, this study con-

tributes significantly to refining models for Archean crustal growth, the tectono-magmatic evolution of the Carajás Province, and the broader understanding of sanukitoid petrogenesis in high-strain settings. A summary of the available geochronological and isotopic data for the sanukitoids from the studied area is provided in Table 1.

6. Analytical techniques

6.1. Sample preparation and scanning electron microscopy

Zircon crystals were extracted from 2 – 5 kg whole-rock samples using a combination of crushing, gravimetric and Frantz magnetic separation techniques. The material was sieved into four size fractions (250, 180, 125 and 75 μm) and subsequently hand-picked under a binocular microscope at the Laboratory of Mineral Preparation, Geoscience Institute, UFPA, Brazil. Approximately 100 zircon grains per sample were mounted in epoxy resin and polished to expose their cores. Internal zircon structures were imaged using a JEOL JXA-8230 scanning electron microscope (SEM) equipped with a Gatan MiniCL system at the Microanalyses Laboratory (UFPA, Brazil) and the Apreo S field-emission (Thermo Scientific, The Netherlands), at the Department of Physics and Astronomy, University of Turku, Turku. U-Pb geochronological analyses were conducted as reported by Nascimento et al. (2024). In a subsequent session, isotopic data were obtained.

6.2. Lu-Hf in zircon isotope by LA-ICP-MS

Zircon Lu–Hf isotopic analyses were performed at Pará–Iso/UFPA using a Thermo-Finnigan Neptune High Resolution Multicollector Inductively Coupled Plasma Mass Spectrometer (HR-MC-ICP-MS) coupled to a Nd: YAG 213 nm New Wave laser ablation system (LSX-213 G2 CETAC laser microprobe). The laser spot size was 30 μm, with an ablation time of 60 s, a repetition rate of 10 Hz, and helium used as the carrier gas. The analytical sequence alternated between zircon samples and the GJ-1 reference zircon, whose $^{176}Hf/^{177}Hf$ ratio is well characterized by solution analysis (0.2820 00 ± 0.000005; 2σ; n = 24; Morel et al., 2008). Lutetium, hafnium, and ytterbium isotopes were measured simultaneously during MC-ICP-MS analysis. Instrumental mass bias was corrected using the exponential law based on the $^{179}Hf/^{180}Hf$ ratio of 0.7325 (Milhomem Neto and Lafon, 2019), following the procedure established at Pará-Iso. The Mud Tank and GJ-1 zircon standards were analyzed as external monitors to assess data accuracy and precision, ensuring the reliability of $^{176}Hf/^{177}Hf$ ratios after mass bias correction. The raw data were processed offline using an Excel-based reduction protocol to calculate the $^{176}Hf/^{177}Hf$ and $^{176}Lu/^{177}$-Hf ratios, the Hf-T^{C}_{DM} model age, and the $\varepsilon_{Hf}(t)$ values for each analytical spot (Supplementary Data Table S1). $\varepsilon_{Hf}(t)$ was calculated using the present-day CHUR values of $^{176}Hf/^{177}Hf$ = 0.282785 and $^{176}Lu/^{177}Hf$ = 0.0336 (Bouvier et al., 2008). Values of $^{176}Lu/^{177}$-Hf = 0.0388 and $^{176}Hf/^{177}Hf$ = 0.28325 were used for the depleted mantle (Andersen et al., 2009), and a $^{176}Lu/^{177}Hf$ ratio of 0.015 was used as the average value for the continental crust to calculate the two-stage crustal Hf model age (Hf-T^{C}_{DM}; DePaolo, 1981; Scherer et al., 2001; Griffin et al., 2002, 2006; Belousova et al., 2010). Additional details about the Lu-Hf methodology developed at Pará-Iso/UFPA can be found in Milhomem Neto and Lafon (2019). Lu-Hf isotopic data are reported in Supplementary Data Table S1.

6.3. Oxygen ($\delta^{18}O$) in zircon isotope by SIMS

Zircon oxygen isotopes analyses were conducted using a Cameca IMS-1280 multicollector ion microprobe via secondary ion mass spectrometry (SIMS) at the NordSIMS facility, National Museum of Natural History, Stockholm, Sweden. Analytical protocols closely follow those reported by Heinonen et al. (2015). A critically focused Cs^+ primary beam with 20 keV impact was used to sputter the sample, and a low-energy electron flooding gun was used for charge compensation. The primary beam current was ca. 2 nA yielding a ca. 15 μm analytical spots, including a 10 μm raster to homogenize the beam profile. Each analysis consisted of an initial pre-sputter over a rastered 20 μm area to remove the gold coating, followed by centering of the secondary beam in the field aperture (field of view on the sample of 30 μm with 90x magnification transmission ion optics). The ^{16}O (ca. 2×10^9 cps) and ^{18}O ion beams were mass filtered at a mass resolution of ca. 2500 (M/ΔM) and analysed simultaneously using two Faraday detectors with, respectively, $10^{10}\Omega$ and $10^{12}\ \Omega$ amplifiers housed in an evacuated, temperature stabilized chamber. The secondary magnet field was locked at high stability using an NMR field sensor operating in regulation mode. All pre-sputter, beam centering and data acquisition steps were automated in the run definition. Typical internal precision obtained for individual run $^{18}O/^{16}O$ ratios was ca. 0.1‰ (SE), based on 12 integrations of 4 s each. Fully automated sequences comprised two measurements of the reference zircon, M257 (Kent, 2008; Nasdala et al., 2008) bracketing six measurements of unknown targets and a secondary reference zircon, Qinghu (Li et al., 2013). The regularly interspersed M257 measurements were used to correct measured isotope ratios for any drift during the analytical session and for instrumental mass fractionation (IMF), assuming $\delta^{18}O_{V\text{-}SMOW}$ = 13.93 ‰. External precision on $\delta^{18}O_{V\text{-}SMOW}$ was 0.11 ‰ and 0.10 ‰ (SD) in the two analytical sessions and is propagated onto the internal precision to yield the overall uncertainty reported in Supplementary Data Table S2. Analyses of the Qinghu zircon yielded averages of 5.05 ‰ ± 0.24 ‰ (2SD, n = 12) and 5.24 ‰ ± 0.36 ‰ (2SD, n = 13) in each of the two sessions, within uncertainty of the value of 5.4 ‰ ± 0.2 ‰ (2SD) reported by Li et al. (2013). $\delta^{18}O$ isotopic data are reported in the Supplementary Table S2.

6.4. Whole-rock Sm-Nd isotope

The whole-rock Sm-Nd analyses were conducted using a Thermo Finnigan Neptune multiple collector ICP-MS (MC-ICP-MS) equipped with Faraday detectors at the Pará-Iso Laboratory (UFPA, Brazil). For each sample, ~100 mg of rock powder was weighed in a Teflon high-pressure vessel, mixed with a $^{150}Nd/^{149}$-Sm tracer solution and HF + HNO_3 acids, and reacted at 150°C, following the procedures described by Oliveira et al. (2008). Post-digestion, the solution was evaporated to dryness and then redissolved in HF + HNO_3 acids. This solution was then dried and taken up in 6 N HCl, followed by sequential drying down and addition of 2 N HCl. Subsequently, rare earth elements (REE) were isolated through ion exchange chromatography using BioRad Dowex 50WX-8 cationic resin, along with 2 N HCl and 3 N HNO_3. Sm and Nd were separated from the other REE and collected by passing the solution through a further set of ion exchange columns loaded with Dowex AGI-X4, 7 N HNO_3 and methanol. After evaporation, each separated Sm and Nd fraction was diluted with 1 mL HNO_3** (2 %) and then analyzed by MC-ICP-MS. During this study, mass fractionation correction for $^{143}Nd/^{144}Nd$ was performed using an exponential law relative to a $^{143}Nd/^{144}Nd$ of 0.7219. The decay constant used was 6.54×10^{-12} $year^{-1}$ (Lugmair and Marti, 1978) and chondritic values used to calculate ε_{Nd} parameter were ^{143}-Nd/^{144}Nd = 0.512638 and $^{147}Sm/^{144}Nd$ = 0.1967 (Ben Othman et al., 1984). Nd model ages (Nd-T_{DM}) for all the samples were calculated using the DePaolo (1981) and DePaolo and Wasserburg (1976) model for a depleted mantle evolution. The La Jolla standard yielded a mean $^{143}Nd/^{144}Nd$ value of 0.511834 ± 0.000005 (n = 6).

Whole-rock Sm-Nd isotopic data are reported in the Supplementary Data Table S3.

6.5. Pb isotope in K-feldspar by LA-ICP-MS

For common Pb in situ isotope measurements, five representative samples with large and clean K-feldspar grains were selected. Thick sections of all samples (25 mm in diameter) were prepared and polished at the Laboratory of Mineral Preparation, University of Turku, Finland. The Pb isotopic ratios ($^{206}Pb/^{204}Pb$, $^{207}Pb/^{204}Pb$, and $^{208}Pb/^{204}Pb$) in alkali feldspar were measured using a Thermo Fisher *Neoma* multicollector inductively coupled plasma mass spectrometer (MC-ICP-MS) coupled to an *Analyte G2* 193 nm ArF excimer laser ablation system at the Laboratory for Isotope Geology, Geological Survey of Finland (GTK), Espoo. The laser operated at a pulse frequency of 10 Hz, with a pulse energy of 5 mJ at 50 % attenuation, producing an energy density of 1.64 J/cm^2 on the sample surface with a 110 μm spot size. Instrumental mass bias was corrected via continuous nebulization of a 2 ppb Tl solution, using the $^{205}Tl/^{203}Tl$ ratio of 2.416 for normalization. The Pb isotopic data were further corrected for isobaric interference of Hg on mass 204. Reported ratios include absolute and propagated 2σ uncertainties (Armistead et al., 2023). Calibration was performed using the NIST SRM 612 silicate glass reference material. The external reproducibility for Pb isotopic ratios on NIST 612 during the analytical sessions was better than ± 0.1 % (2SD), consistent with values reported in the literature (Kent, 2008), thereby confirming the accuracy and reliability of the results. Analyses yielding Pb signals lower than 100 mV on mass 208 were discarded due to insufficient signal intensity. Analytical results of Pb isotopes in K-feldspar are provided in the Supplementary Data Table S4.

6.6. Geochemical modelling

Geochemical modeling involves three steps. In the first step, a simple mixing model was applied between the tonalite from the basement of the studied area (Santos et al., 2018) and the primitive mantle (McDonough, 2014) to represent an enriched metasomatized mantle. Binary mixing calculations followed the equation: $X_M = X_A f + X_B(1-f)$, where X_A and X_B are the concentrations of the elements or oxides in the end members, X_M is the element or oxide content in the calculated mixture, and f is an index described by A/(A + B) (Armistead et al., 2023). The starting compositions for the modelling are provided in the Supplementary Data Table S5. In the second step, the residual mineral assemblage was modeled to replicate the expected melt composition using the software GENESIS 4.0 (Janoušek et al., 2015). In this stage, mineral chemistry data for garnet, orthopyroxene, clinopyroxene, phlogopite, magnetite, plagioclase, and muscovite were sourced from Rapp et al. (2010), Leite (2001), and Moyen et al. (2001), considering a garnet peridotite source composition. The mineral–liquid partition coefficients used for trace element modeling were obtained from the Geochemical Earth Reference Model (GERM) database (https://kdd.earthref.org/KdD/) (Supplementary Data Table S6). The modeled data are considered reliable when the sum of the squared residuals (ΣR^2) is ≤ 1.2 (Albaréde, 1995; Ersoy and Helvaci, 2010; Janoušek et al., 2015). In the third step, a batch melting model was employed to simulate the composition of sanukitoid melts extracted from the enriched mantle (as defined in step 1), using the mineralogical compositions modeled in step 2. An in-house Excel spreadsheet was used to calculate modeled trace element concentrations based on the batch melting equation: $C_L/C_o = 1/D(1-F)^{(1/D-1)}$, where C_L and C_o are the trace element concentrations in the melt (liquid) and the source (solid), respectively (Albaréde, 1995). F is the weight fraction of the melt formed, and D is the bulk distribution coefficient for the residual solids at the moment when the melt is removed from the system.

For the isotopic modeling involving Nd, Hf, Pb, and O systems, a mixing model was applied to evaluate the contributions to the reservoirs source (Supplementary Data Table S7). The endmembers considered include one depleted mantle reservoir (Workman and Hart, 2005) and three distinct metasomatic agents: (1) melts derived from subducted sediments (Plank and Langmuir, 1998), (2) slab-derived hydrous fluids (Plank and Langmuir, 1998), and (3) TTG-type silicic melts (Santos et al., 2018). Oxygen isotope values were assumed to follow mantle-like or TTG-derived ranges as appropriate. Zircon $\delta^{18}O$ values below 5.0‰, recorded in a subset of grains, were excluded due to clear evidence of alteration (inclusions, fractures). Similarly, anomalously radiogenic Pb isotope data in K-feldspar grains with visible alteration halos were removed from modeling datasets. The parameters used in the calculations are provided in the Supplementary Data Table S7.

7. Results

7.1. Lu-Hf in zircon

The zircon Hf isotope data for the Bt-Amp granodiorite of the Água Limpa pluton (sample ADK-39) were obtained from 12 spots within zircon domains exhibiting the same or similar internal structure as those analyzed for U-Pb SHRIMP dating (Nascimento et al., 2024). For this study, all the Hf isotopic measurements were performed on zircons with over 95 % concordance on U-Pb ages (Supplementary Data Table S1). The $^{176}Hf/^{177}Hf_{(2.87\ Ga)}$ ratios yielded values ranging from 0.280896 to 0.280982. The $\varepsilon_{Hf(2.87\ Ga)}$ values calculated from their crystallization ages ranged from –1.41 to +1.65 (Fig. 5a), with Mesoarchean Hf-T^C_{DM} model ages varying from 3.01 Ga to 3.18 Ga (Fig. 5a). Similarly, for the Amp-Bt tonalite of the Água Limpa pluton (sample SE-17A), 13 spots Hf isotope analysis were conducted on selected zircons, with initial $^{176}Hf/^{177}Hf_{(2.87\ Ga)}$ ratios ranging from 0.280842 to 0.280993 and $\varepsilon_{Hf(2.87\ Ga)}$ values from –3.31 to +2.06. The Hf-T^C_{DM} model ages for these zircons ranged from 2.98 Ga to 3.28 Ga (Fig. 5a).

Zircon grains from the Água Azul pluton (samples SE-94 and EDC-76) were also analyzed for Lu-Hf isotopes (Supplementary Data Table S1). The Ep-Amp-Bt granodiorite (sample SE-94) displayed initial $^{176}Hf/^{177}Hf_{(2.87\ Ga)}$ ratios between 0.280942 and 0.280994 and $\varepsilon_{Hf(2.87\ Ga)}$ values from + 0.27 to + 2.14 (Fig. 5a), with Mesoarchean Hf-T^C_{DM} model ages ranging from 2.98 Ga to 3.08 Ga. Similarly, the Ep-Amp-Bt tonalite (sample EDC-76) exhibited initial $^{176}Hf/^{177}Hf_{(2.87\ Ga)}$ ratios between 0.280938 and 0.280982 and $\varepsilon_{Hf(2.87\ Ga)}$ values from + 0.08 to + 1.65 (Fig. 5a), with Mesoarchean Hf-T^C_{DM} model ages from 3.01 Ga to 3.09 Ga.

7.2. $\delta^{18}O$ isotope in zircon

The oxygen isotopic results of zircon obtained via SIMS are presented in Fig. 5b. A total of 188 analyses were conducted on zircons from six distinct varieties of sanukitoids belonging to the Água Limpa Suite (Supplementary Data Table S2). These include three samples from the Água Limpa Pluton (ADK-39, SE-22A, and SE-17A) and three from the Água Azul Pluton (EDC-74A, EDC-76, and SDA-01). All zircon domains exhibit > 95 % age concordance (Nascimento et al., 2024).

Among the screened analyses, 139 display mantle-like to elevated $\delta^{18}O$ values, with weighted mean $\delta^{18}O$ values ranging from + 5.03 ‰ ± 0.01 ‰ to + 7.61 ‰ ± 0.01 ‰. For the biotite-amphibole granodiorite sample ADK-39, 31 analyses yielded $\delta^{18}O$ values between + 5.25 ‰ and + 6.76 ‰. Sample SE-22A underwent 30 analyses, showing $\delta^{18}O$ values ranging from + 5.10 ‰ to + 6.7

Table 1
Summary of geochronological and isotopic data for the sanukitoids of the Sapucaia Subdomain, Carajás Province, Amazonian Craton.

Sample	Location (UTM)		Rock type	Age	2sig	$^{176}Hf/^{177}Hf_{(t)}$	$\varepsilon_{Hf}(t)$	2sig	T^{C}_{DM} (Ga)	$\delta^{18}O$	Sm	2sig	Nd	2sig	$^{147}Sm/^{144}Nd$	2sig	$^{143}/^{144}Nd$	2sig	$\varepsilon_{Nd}(t)$	Nd-T_{DM}	$^{206}Pb/^{204}Pb$ (t)	$^{207}Pb/^{204}Pb$ (t)	$^{208}Pb/^{204}Pb$ (t)
	Northing	Easting		(Ma)	(95 %)			(95 %)			(ppm)	sd	(ppm)	sd		sd		sd					
Água Limpa pluton																							
ADK-39	9,262,332	589,600	granodiorite	2870 ± 4	1.6	0.280896 to 0.280992	−1.4 to 1.6	1.0	3.0 to 3.2	2.8 to 6.9	3.15	0.5	19.31	0.5	0.0985	9	0.51070	9	−1.64	3.1	14.14 to 14.60	15.15 to 15.50	33.15 to 33.82
SE-17A	9,258,605	580,625	tonalite	2870*	–	0.280842 to 0.280993	−3.3 to 2.0	0.7	2.9 to 3.0	3.0 to 6.8	3.05	0.6	20.67	0.6	0.08926	14	0.51062	14	0.39	3.0	–	–	–
SE-22A	9,259,897	577,526	granodiorite	2870*	–	–	–	–	–	3.4 to 6.7	3.02	0.5	23.33	0.5	0.0782	6	0.51045	6	1.17	2.9	–	–	–
ADK-70	9,259,958	581,663	granodiorite	2870*	–	–	–	–	–	–	–	–	–	–	–	–	–	–	–	–	13.64 to 19.05	14.80 to 18.70	33.20 to 42.60
EDC-12C	9,249,384	579,591	granodiorite	2870*	–	–	–	–	–	–	–	–	–	–	–	–	–	–	–	–	13.25 to 14.69	14.51 to 15.55	32.59 to 35.30
Água Azul pluton																							
SE-94	9,247,789	575,492	granodiorite	2872 ± 5	0.78	0.280949 to 0.280994	0.2 to 2.1	1.0	2.9 to 3.0	–	–	–	–	–	–	–	–	–	–	–	–	–	–
SE-14	9,253,167	578,557	granodiorite	2870*	–	–	–	–	–	–	5.0	0.6	29.06	0.6	0.10393	48	0.51090	48	0.37	3.0	–	–	–
SE-51	9,249,482	570,536	granodiorite	2870*	–	–	–	–	–	–	3.21	0.6	18.31	0.6	0.10590	41	0.51089	41	−0.62	3.0	–	–	–
EDC-76	9,247,938	556,123	tonalite	2870 ± 4	0.30	0.280940 to 0.280982	0.1 to 1.6	1.0	3.0	4.9 to 7.6	2.77	0.5	19.67	0.5	0.09507	7	0.51074	7	0.5	2.9	–	–	–
EDC-74A	9,249,090	562,815	monzogranite	2887 ± 9	1.8	–	–	–	–	1.5 to 6.5	–	–	–	–	–	–	–	–	–	–	–	–	–
SDA-01	9,250,586	571,090	monzogranite	2870*	–	–	–	–	–	3.2 to 6.5	4.18	0.6	25.98	0.6	0.09724	11	0.51076	11	0.11	3.0	–	–	–
EDC-75	9,247,880	555,454	granodiorite	2870*	–	–	–	–	–	–	–	–	–	–	–	–	–	–	–	–	16.31 to 18.27	16.72 to 17.61	34.64 to 36.56
EDC-71	9,249,060	563,660	monzogranite	2870*	–	–	–	–	–	–	–	–	–	–	–	–	–	–	–	–	14.44 to 15.07	15.37 to 16.23	33.64 to 36.18
EDC-08	9,253,656	551,322	granodiorite	2870*	–	–	–	–	–	–	3.04	0.5	24.03	0.5	0.07658	9	0.51045	9	1.76	2.9	–	–	–

Note: * Inferred age.

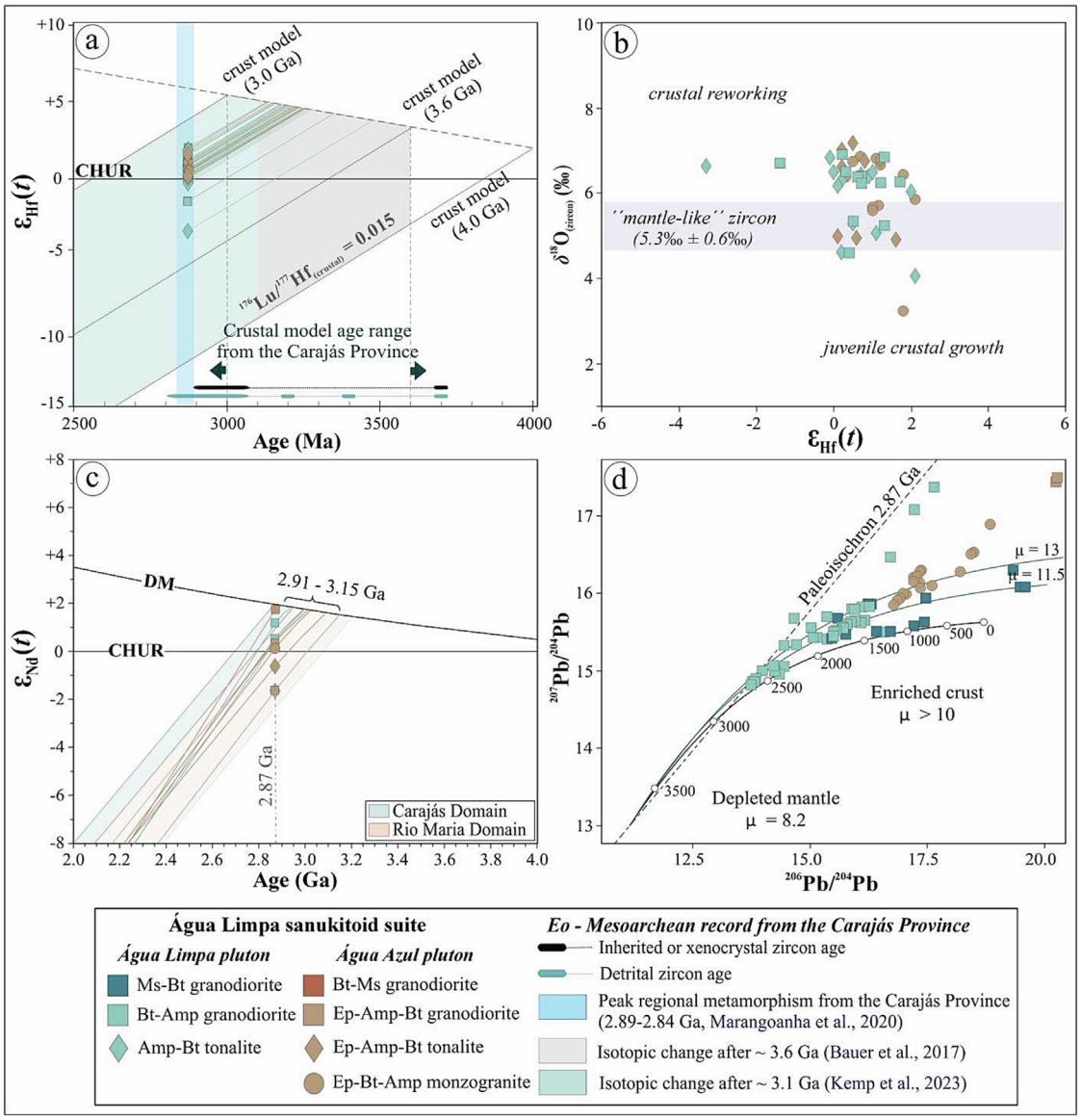

Fig. 5. Isotopic data for the Mesoarchean Água Limpa sanukitoid suite. (a) $\varepsilon_{Hf}(t)$ vs. age (Ma) evolution diagram, (b) $\delta^{18}O$ (zircon) ‰ vs. $\varepsilon_{Hf}(t)$, (c) $\varepsilon_{Nd}(t)$ vs. age (Ga), and (d) $^{207}Pb/^{204}Pb$ vs. $^{206}Pb/^{204}Pb$ ratios for the K-feldspar along with the Stacey and Kramers (1975) evolution curve. Two single-stage growth curves for fixed μ value ($^{232}Th/^{238}U$) of 11.5 and 13 are shown for reference. The mantle zircon value is from Valley et al. (2005). The present-day parameters for the CHUR and DM models were taken from Bouvier et al. (2008) and Andersen et al. (2009), respectively. The crustal evolutionary trend (0.015) is from Griffin et al. (2006) and Belousova et al. (2010). Peak regional metamorphism at 2.89–2.84 Ga (Marangoanha et al., 2020). Isotopic shifts after ~ 3.6 Ga and ~ 3.1 Ga are from Bauer et al. (2017) and Kemp et al. (2023), respectively. Abbreviations: CHUR = Chondritic Uniform Reservoir; DM = Depleted Mantle.

0 ‰. Similarly, the amphibole-biotite tonalite sample SE-17A was subjected to 35 analyses, which revealed $\delta^{18}O$ values varying from + 5.04 ‰ to + 6.89 ‰. In the Água Azul Pluton, the amphibole-epidote-biotite monzogranite sample EDC-74A yielded 35 analyses, with $\delta^{18}O$ values ranging from + 5.03 ‰ to + 6.65 ‰. Another monzogranite sample, SDA-01, from the same pluton showed $\delta^{18}O$ values between + 5.12 ‰ and + 7.10 ‰. The amphibole-epidote-biotite tonalite sample EDC-76 yielded $\delta^{18}O$ values ranging from + 5.13 ‰ to + 7.61 ‰ (Supplementary Data Table S2). The majority of analyses plot within the crustal reworking field on the $\varepsilon_{Hf}(t)$ vs. $\delta^{18}O_{zircon}$ (‰) diagram (Fig. 5b).

7.3. Whole-rock Sm-Nd

Whole-rock Sm-Nd data for the Água Limpa Suite sanukitoids are listed in the Supplementary Data Table S3 and illustrated in an $\varepsilon_{Nd}(t)$ vs. Age (Ga) evolution diagram (Fig. 5c). Assuming a crystallization age of 2.87 Ga (Nascimento et al., 2024), the initial $^{143}Nd/^{144}Nd$ values fall between 0.510450 and 0.510899 across all samples of sanukitoids. Suprachondritic to subchondritic $\varepsilon_{Nd}(t)$ values (+1.17 to –1.64) and Mesoarchean model ages (Nd-T_{DM} = 2.94 – 3.15 Ga) were obtained for the Água Limpa pluton. In contrast, the Água Azul pluton showed $\varepsilon_{Nd}(t)$ values ranging from + 1.76 to –0.62, with Mesoarchean Nd-T_{DM} ages between 3.09 Ga and 2.91 Ga.

7.4. Pb isotope in feldspar

A total of 109 single K-feldspar grains were analyzed from the sanukitoids samples of the Água Limpa suite (Supplementary Data Table S4). These include three samples from the Água Limpa pluton (samples ADK-39, ADK-70 and EDC-12C) and two from the Água

Azul pluton (samples EDC-75 and EDC-71). Their Pb isotopes are shown in Fig. 5d, alongside the evolution curve for the Bulk Silicate Earth ($\mu > 10$, $\kappa = 4.05$; Stacey and Kramers, 1975; Armistead et al., 2023) and the primitive mantle ($\mu = 8.2$, $\kappa = 4.21$).

In the Água Limpa pluton, K-feldspar grains from the biotite-amphibole granodiorite facies (AKD-39 and ADK-70) exhibit age-corrected Pb isotope compositions ranging from 13.64 < $^{206}Pb/^{204}Pb$ < 19.05, 14.79 < $^{207}Pb/^{204}Pb$ < 18.70, and 36.15 < $^{208}Pb/^{204}Pb$ < 42.60. The muscovite-biotite granodiorite (EDC-12C) displays ratios of 13.25 < $^{206}Pb/^{204}Pb$ < 14.69, 14.51 < $^{207}Pb/^{204}Pb$ < 15.55, and 32.59 < $^{208}Pb/^{204}Pb$ < 35.30. For the Água Azul pluton, K-feldspar grains from the epidote-amphibole-biotite granodiorite (EDC-75) show values of 16.30 < $^{206}Pb/^{204}Pb$ < 18.27, 16.78 < $^{207}Pb/^{204}Pb$ < 18.13, and 34.64 < $^{208}Pb/^{204}Pb$ < 35.86. Similarly, those from the amphibole-epidote-biotite monzogranite (EDC-71) exhibit ratios of 14.44 < $^{206}Pb/^{204}Pb$ < 15.63, 15.37 < $^{207}Pb/^{204}Pb$ < 16.23, and 34.65 < $^{208}Pb/^{204}Pb$ < 34.92.

Overall, the Pb isotopic results from all five samples form a tight, linear array extending from $^{207}Pb/^{204}Pb$ of 14.8 to 18.7, corresponding to μ ($^{238}U/^{204}Pb$) values between 11.5 and 15.0. These results align well with enriched crust Pb evolution frameworks (Fig. 5d). Pb model ages calculated using the two-stage Stacey and Kramers (1975) model yield ages for the K-feldspar grains that are 2.0 Ga to 3.5 Ga younger (on average, > 2.0 Ga) than the established U-Pb crystallization ages from the Água Limpa suite sanukitoids (Nascimento et al., 2024).

7.5. Geochemical modelling

Previously proposed genetic models for the granodiorite and tonalite varieties of the Água Limpa and Água Azul sanukitoid-affinity plutons suggest ~ 20% partial melting of subcontinental lithospheric mantle (SCLM) enriched by ~ 30% TTG-type melt. These models assume a residual mineral assemblage of garnet, orthopyroxene, clinopyroxene, and magnetite, indicating significant crust–mantle interaction (Nascimento et al., 2024). However, they do not account for the muscovite-bearing and monzogranite varieties, which display distinct geochemical signatures in most diagrams, implying a more evolved or variably modified source.

To refine the interpretation of the mantle source for all sanukitoid varieties in the Água Limpa suite, new geochemical modeling was conducted for the muscovite-bearing and monzogranite types (Supplementary Data Table S8). This analysis evaluated whether their compositional differences result from variations in the inherited source, distinct metasomatic agents, or increased crustal assimilation during magma ascent. The metasomatized mantle source was modeled as a binary mixture of primitive mantle (McDonough, 2014) and a local TTG-type tonalite (Santos et al., 2018), with residual mineral compositions derived from Moyen et al. (2001), Rapp et al. (2010), and Leite (2001).

Results indicate that the muscovite-bearing and monzogranite varieties formed via 11 % – 15 % equilibrium partial melting of SCLM enriched by 30 % – 32 % TTG-type melt (Fig. 6). The residual assemblage comprises orthopyroxene (58.6 % – 59.8 %), garnet (23.5 % – 24.1 %), clinopyroxene (9.2 % – 10.1 %), phlogopite (5.8 % – 6.9 %), and magnetite (0.9 % – 1.3 %), with $\Sigma R^2 < 1$.

8. Discussion

8.1. Geochemical and isotopic constraints on reservoir source: Evidence of crustal assimilation

The petrogenesis of the Água Limpa and Água Azul plutons is constrained by a combination of geochemical signatures and isotopic systematics that collectively point to a complex magmatic history. Three key observations emerge as factual constraints: (i) Geochemical affinity to sanukitoids: all granitoid varieties — tonalite, granodiorite, monzogranite, and muscovite-bearing types — exhibit high Mg# contents (Mg# = 45 – 65), enrichments in LILEs (e.g., Ba > 700 ppm, Sr > 800 ppm), Cr (> 200 ppm), Ni (> 100 ppm) and positive trends in LREE, along with Nb–Ta and HREE depletions (Gabriel and Oliveira, 2014; Nascimento et al., 2024). The presence of phlogopite in the residue further supports a K-rich, hydrous, and oxidized mantle source (Hermann et al., 2006). The residual mineralogy obtained through modeling suggests that, in addition to TTG-derived silicic melt metasomatism — primarily contributing Na and Si — the mantle source was modified by hydrous fluids or melts enriched in K and LILEs. Such metasomatic agents are typically sourced from the dehydration of altered oceanic crust, common in convergent margin settings (Laurent et al., 2014). These traits match the geochemical fingerprint of Archean sanukitoids and indicate derivation from a metasomatized mantle source. (ii) Isotopic (Nd-Hf-O-Pb) evidence show that the studied sanukitoids were not derived solely from depleted mantle sources but contain significant amounts of crustal input ($\varepsilon_{Nd}(t)$ values ranging from −1.64 to + 1.76, and $\varepsilon_{Hf}(t)$ from −3.31 to + 2.06), placing most samples near CHUR and significantly away from depleted mantle (DM) trends. Corresponding T_{DM} ages of 2.98 – 3.28 Ga and zircon $\delta^{18}O$ values up to 6.0‰ confirm involvement of older supracrustal components, either inherited or assimilated. Pb isotopes (e.g., high $\mu > 10$ in K-feldspar) also reflect an enriched, evolved source. (iii) Textural and chemical indicators of crustal modification: the muscovite-bearing granodiorites, characterized by high Al_2O_3 (>15 wt.%) and elevated SiO_2 (>62 wt.%), differ from the tonalitic and granodioritic varieties (Nascimento et al., 2024). These geochemical distinctions imply progressive crustal assimilation (Fig. 7).

To evaluate the origin of the crustal isotopic signature, two main models were tested. The first model refers to the metasomatized mantle with subducted sediment input. However, isotopic mixing models using plots of $^{208}Pb/^{204}Pb$ versus $^{206}Pb/^{204}Pb$ and $\varepsilon_{Hf}(t)$ versus $\varepsilon_{Nd}(t)$ show that mixing of bulk sediment or sediment-derived fluids with DM fails to reproduce the high Th/Nd ratios (>0.50), negative to positive $\varepsilon_{Nd}(t)$ and $\varepsilon_{Hf}(t)$ observed in the Água Limpa suite sanukitoids (Fig. 8a-c). For instance, Pb–Pb isotope arrays ($^{208}Pb/^{204}Pb$ vs. $^{206}Pb/^{204}Pb$) predicted by sediment-DM mixing exceed observed ratios and mixing vectors on εHf–εNd diagrams plot outside the samples field. Therefore, the geochemical fingerprint does not support significant involvement of subducted sediment-derived melts. Based on the lack of diagnostic sediment melt signatures (e.g., low Th/U, negative ΔNd isotope), we conclude that such input was negligible or absent in the source region. The second model refers to the crustal assimilation and/or contamination by the ancient continental crust (Fig. 8c-f). A more consistent interpretation arises from a two-stage model involving: (1) source hybridization: the mantle was metasomatized by ~ 30% TTG-type melt (Santos et al., 2018), derived from melting of older crustal material; yielding an enriched source, which corroborates with the geochemical modelling that simulated equilibrium partial melting of a TTG-enriched mantle source (Fig. 8c). These results ($\Sigma R^2 < 1.0$) closely match observed trace element patterns of the studied sanukitoids, especially for Sr, Ba, Th, Nb, and REE profiles (Nascimento et al., 2024). However, the enrichment in K, Ba, and Sr also suggests subsequent interaction with LILE-rich hydrous fluids. Moreover, the possibility of interaction with the upwelling asthenosphere is indirectly supported by the hybrid trace element signature (e.g., elevated HFSEs relative to TTGs) and overall melt fertility. (2) Shallow-level crustal assimilation: isotopic variations between Água Limpa-Água Azul sanukitoid plutons, especially lower $\varepsilon_{Nd}(t)$, $\varepsilon_{Hf}(t)$, and higher $\delta^{18}O$ values in the Água Limpa samples compared to the Água Azul pluton, sug-

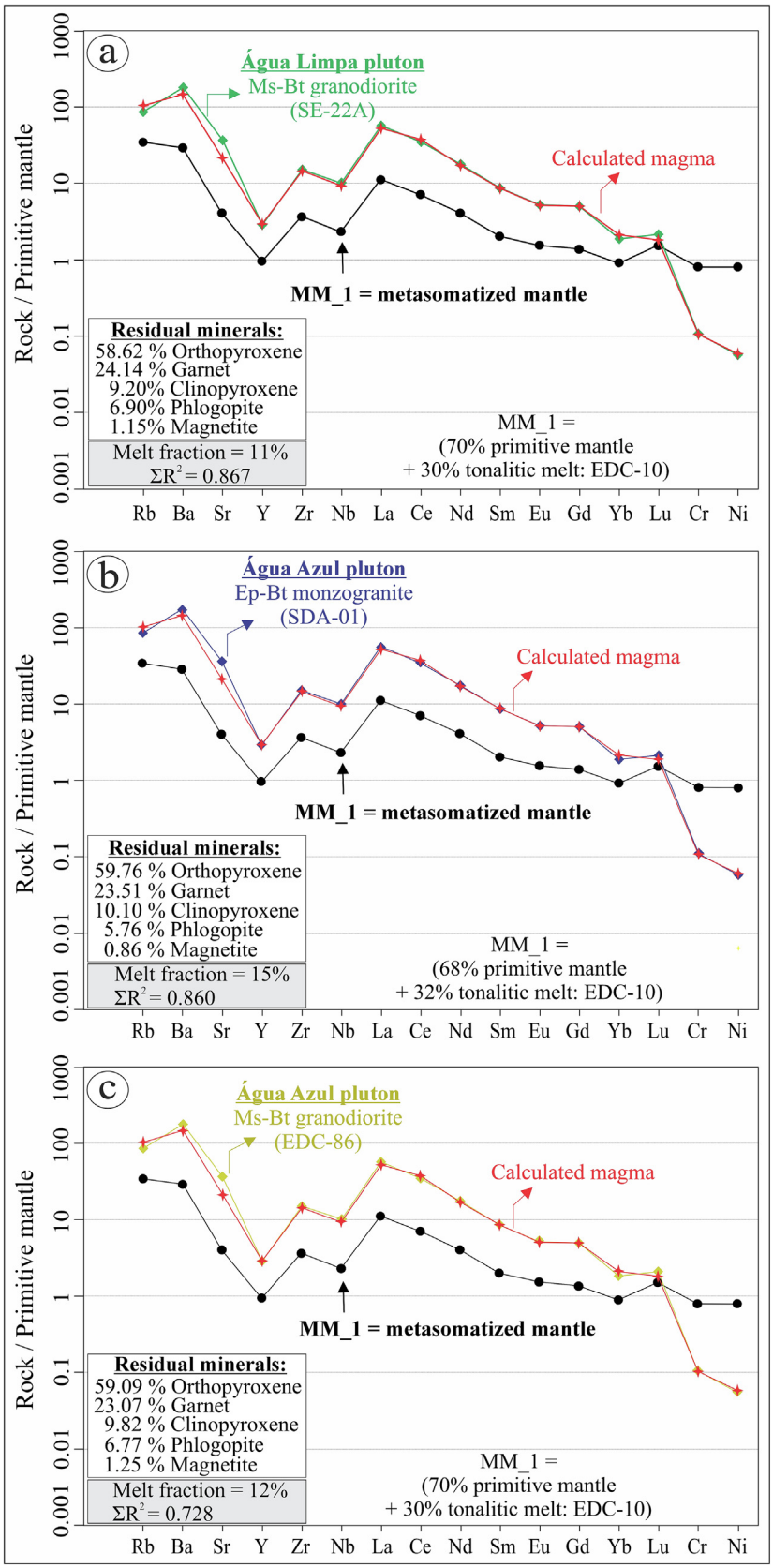

Fig. 6. Results of mixing modelling to explain the sanukitoid trace element composition of the Água Limpa sanukitoid suite. Água Limpa pluton: (a) muscovite-biotite granodiorite. Água Azul pluton: (b) epidote-biotite monzogranite; (c) muscovite-biotite granodiorite. Normalization values for the primitive mantle (McDonough, 2014).

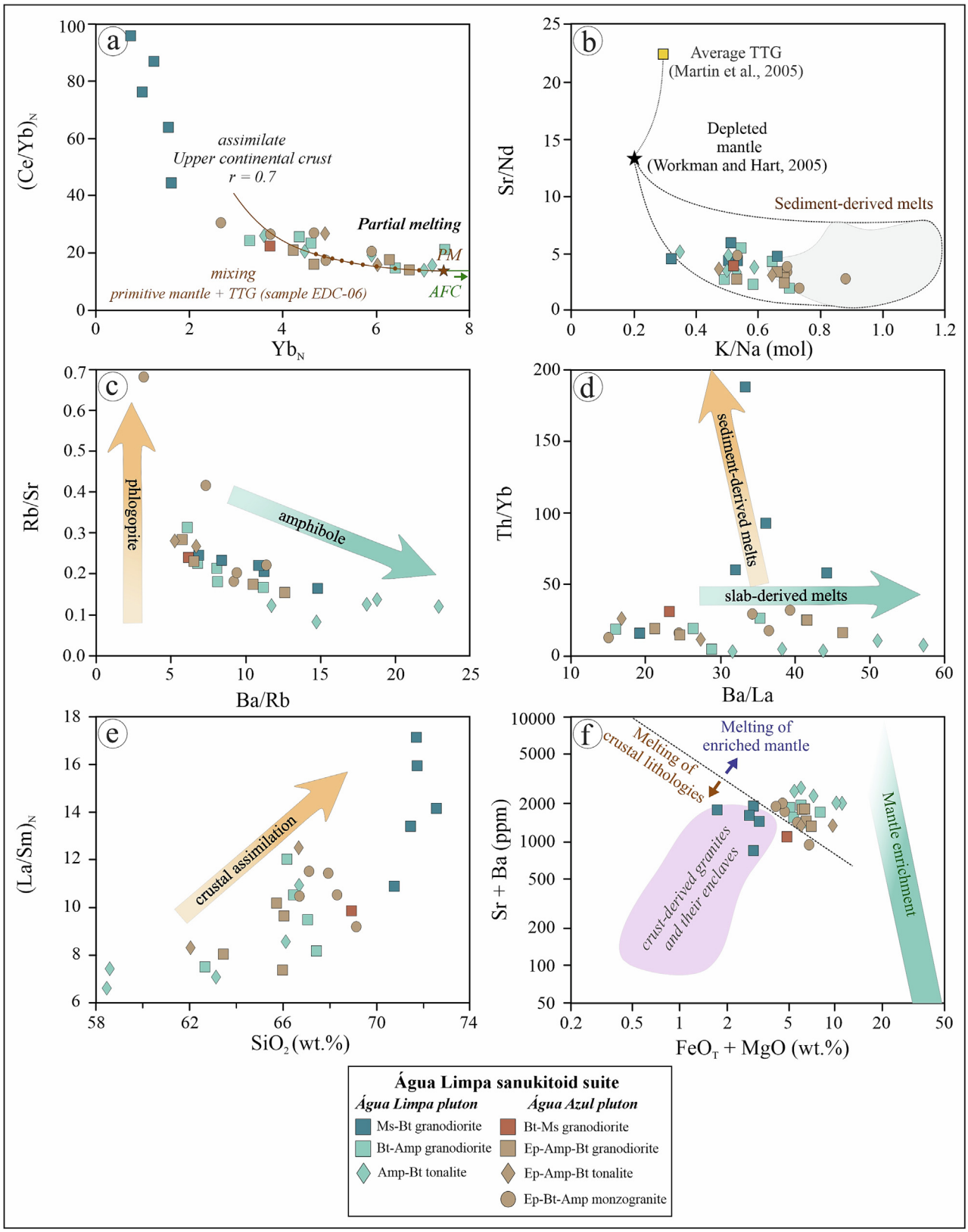

Fig. 7. Nature of mantle source and overprint for the Água Limpa sanukitoid suite: (a) $(Ce/Yb)_N$ vs. Yb_N; (b) Sr/Nd vs. K/Na; (c) Rb/Sr vs. Ba/Rb; (d) Th/Yb vs. Ba/La; (e) $(La/Sm)_N$ vs. SiO_2 (wt.%); (f) Sr + Ba vs. FeO_T + MgO (wt.%). Abbreviations: PM = partial melting; AFC = assimilation and fractional crystallization; TTG = tonalite-trondhjemite-granodiorite.

gest varying degrees of assimilation during ascent through the ancient Amazonian upper crust. Further modeling using three crustal reservoirs—lower crust, sediment-derived melt, and bulk continental crust — suggests that the crustal contribution to the

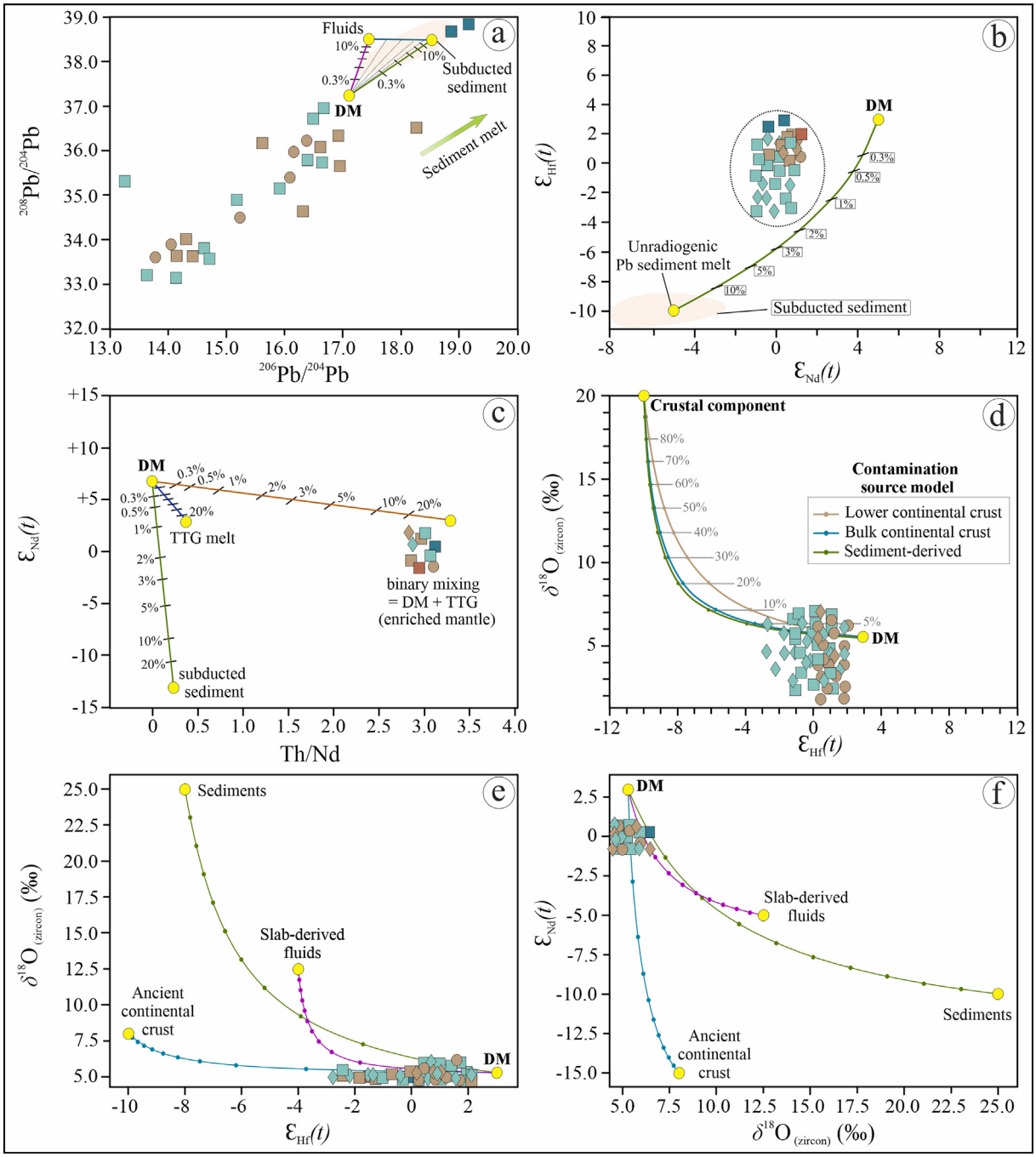

Fig. 8. Pb-Hf-Nd-O isotopic modelling of recycled components and its relationship with mantle. DM trace element concentrations are from Vervoort et al. (2011) and references therein. The composition of the ancient continental crust is based on the data of Workman and Hart (2005) and Plank and Langmuir (1998). The compositions of the slab-derived fluids are based on 0 % – 20 % recycled sediment and 80 % – 100 % upper oceanic crust of Valley et al. (1998) and references therein. Other parameters used in the mixing calculation can be found in Valley et al. (1998), Johnson and Plank (1999), Eiler (2001), Kessel et al. (2005), Chauvel et al. (2008), and Song et al. (2013). (a) $^{208}Pb/^{204}Pb$ vs. $^{206}Pb/^{204}Pb$ in K-feldspar; (b) plot of $\varepsilon_{Hf}(t)$ vs. $\varepsilon_{Nd}(t)$; (c) $\varepsilon_{Nd}(t)$ vs. Th/Nd; (d) and (e) plot of $\delta^{18}O_{(zircon)}$ vs. $\varepsilon_{Hf}(t)$; (f) plot of $\delta^{18}O_{(zircon)}$ vs. $\varepsilon_{Nd}(t)$ average.

hybrid source is typically around 10 % – 5 % assimilation of evolved crust ($\varepsilon_{Nd}(t) \approx -5$, $\varepsilon_{Hf}(t) \approx -2$, $\delta^{18}O \approx 7.5‰$) which is sufficient to reproduce the isotopic characteristics of the Água Limpa-Água Azul sanukitoids (Fig. 8d, e, f). High-Al contents in muscovite-bearing granodiorites (>15 wt.%) and the presence of peraluminous minerals such as muscovite and phlogopite as residual phase provide further petrochemical evidence for crustal assimilation.

The Água Limpa–Água Azul sanukitoids exemplifies a magmatic regime where deep mantle-derived melts hybridized with ancient crustal material both in the source and during ascent. The observed isotopic heterogeneity reflects the combined influence of TTG-derived melts, hydrous metasomatic fluids, and crustal assimilation in modifying the mantle source. Hf model ages and elevated $\delta^{18}O$ values corroborates that crustal recycling processes intensified after 2.87 Ga, consistent with global Archean trends (Fig. 9).

8.2. The change in geodynamic regime at the end of the Mesoarchean

The deformation patterns observed in Archean terrains have long been a subject of scientific debate (Choukroune et al., 1997;

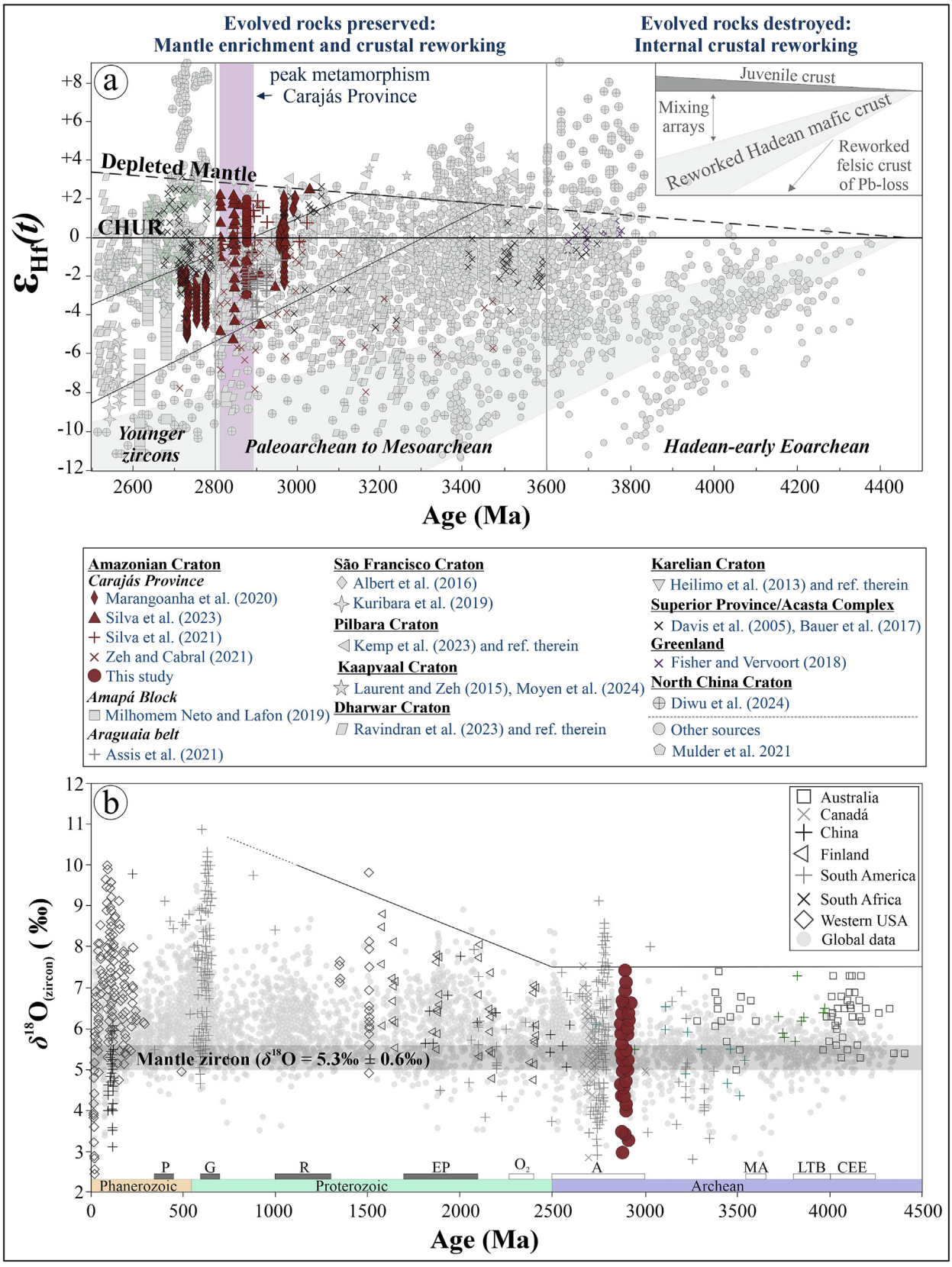

Fig. 9. Comparison of Hf-oxygen isotope data from the Amazonian Craton with selected global sources: (a) $\varepsilon_{Hf}(t)$ vs. Age (Ma), with global data compiled from Mulder et al. (2021) and references therein; (b) $\delta^{18}O$ ‰ versus Age (Ma) for zircons from rocks with known age (Valley et al., 2005). Periods of supercontinent growth are shown by short bars at bottom: P = Pangea; G = Gondwana; R = Rodinia, EP = Early Proterozoic; A = Archean; and MA = Middle Archean. LTB = Late Terminal bombardment, CEE = Cool Early Earth, and O_2 = rise of oxygen in the atmosphere. The mantle zircon value is sourced from Valley et al. (2005). The present-day parameters for the CHUR and DM models were taken from Bouvier et al. (2008) and Andersen et al. (2009), respectively. The crustal evolutionary trend is from Griffin et al. (2006) and Belousova et al. (2010). Compiled sources: Amazonian craton [Carajás province: Marangoanha et al., 2020; Silva et al., 2021, 2023; Zeh and Cabral, 2021]; Amapá Block (Milhomem Neto and Lafon, 2019); Araguaia belt (Assis et al., 2021); São Francisco craton (Albert et al., 2016; Kuribara et al., 2019); ; Pilbara craton (Kemp et al., 2023); Kaapvaal craton (Laurent and Zeh, 2015; Moyen et al., 2024); Dharwar craton (Ravindran et al., 2023); Karelian craton (Heilimo et al., 2013); Superior province/Acasta complex (Davis et al., 2005; Bauer et al., 2017); Greenland (Fisher and Vervoort, 2018); North China craton (Diwu et al., 2024); Other sources (Mulder et al., 2021).

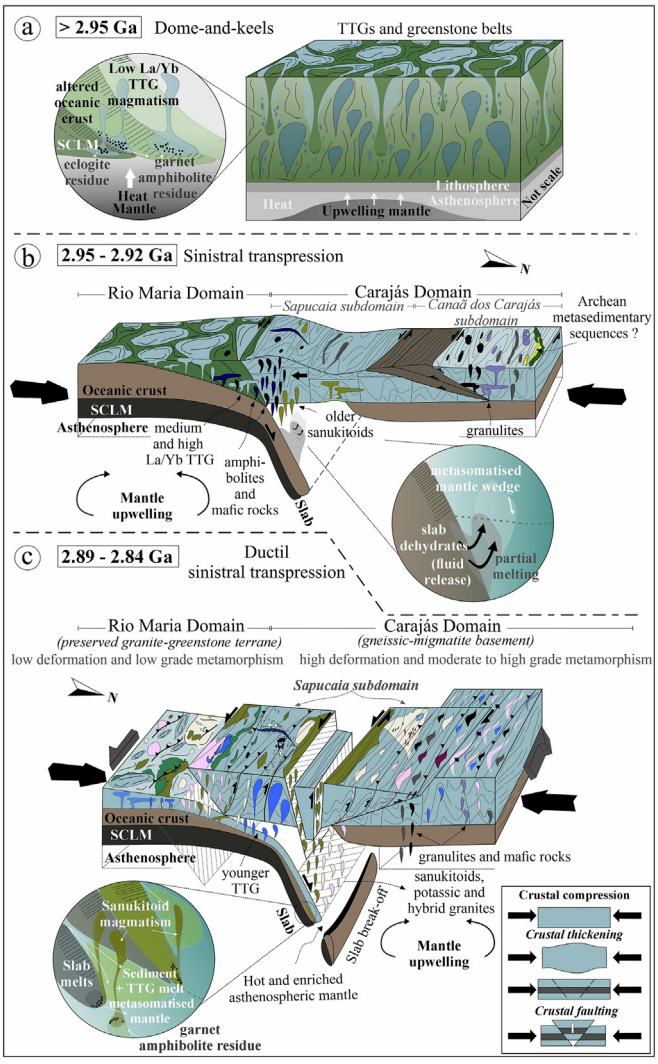

Fig. 10. Proposed geotectonic model for the Archean crust of the Sapucaia Subdomain. (a) Dome-and-keels setting (**> 2.95 Ga**): The initial phase is characterized by sagduction, drip-tectonics, or vertical tectonics, leading to the formation of greenstone belt sequences. The partial melting of basalts (altered oceanic crust), transformed into amphibolites, generated tonalite-trondhjemite-granodiorite (TTG) magmas. The ascent of these magmas intruded into the greenstone sequences, resulting in the characteristic domes-and-keels structural configuration. (b) Transitional tectonic regime (**2.95 – 2.92 Ga**): This phase marks a progressive transition in the tectonic regime. The collision between the Carajás Domain and the Rio Maria Domain induced continuous crustal thickening, faulting and the onset of subduction processes. A propagation of E-W-oriented shear zones, predominantly dipping southward, was accompanied by the emplacement of TTG magmas and amphibolites. Sanukitoid magmatism, although limited, is documented at approximately 2.92 Ga. (c) Subduction (**2.89 – 2.84 Ga**): Following a period of tectonic quiescence, subduction processes became more effective. During this phase, the Sapucaia Subdomain crust underwent exhumation, and concurrent with this activity, granulitic rocks from the lower crust were uplifted and the older TTG basement (migmatized gneisses) underwent reworking. Around 2.87 Ga, partial melting of an enriched mantle produced Mg-rich parental magmas of the Água Limpa suite sanukitoids. After 2.87 Ga, the melting of TTG granitoids at the base of the crust generated granitic liquids. The reactivation of shear zones facilitated interactions between compositionally distinct magmas, resulting in the formation of hybrid granitoids. Abbreviation: SCLM = Subcontinental Lithospheric Mantle.

Polat et al., 2015). A central issue revolves around the tectonic mechanisms responsible for the geometric configuration of granite-greenstone terrains and the processes involved in the formation of sanukitoids and other calc-alkaline granites within Archean cratons (Laurent et al., 2014). Some researchers attribute the shift in granitoid chemistry — from TTGs to late calc-alkaline granites — to the onset of modern-style tectonics (Cawood et al., 2018; Palin et al., 2020). However, others argue that this shift could occur in a non-subductive setting (Nebel et al., 2018; Mole et al., 2019). In the Carajás Province, recent studies suggest that a period of drip tectonics (vertical tectonics or sagduction) could promote metasomatism of the sub-continental lithospheric mantle (SCLM), implying that the presence of sanukitoids and K-granites does not necessarily require prior subduction processes (Costa et al., 2020). Conversely, other studies attribute this geochemical transition to the onset of a subduction regime in the province (Leite et al., 2004; Marangoanha et al., 2020; Silva et al., 2023). This study highlights that the dichotomy between vertical and horizontal tectonic models underscores the complexity of Archean crustal evolution, with both mechanisms potentially contributing to the observed geological and structural patterns in the Carajás Province during distinct periods. According to Li et al. (2018) and Sun et al. (2025), microplates may also have played an important role in that transitional tectonic regime.

The Carajás Province consists of two tectonic domains: Rio Maria (3.07 – 2.93 Ga) and Carajás (3.07 – 2.70 Ga; age of crystallization). Rio Maria features low-grade granite-greenstone terrains with dome-and-keel structures (Fig. 10a), while Carajás is a high-grade gneiss terrain with intense east–west shearing (Marangoanha et al., 2020; Silva et al., 2023). Their structural contrast results from a Mesoarchean north–south collision, which caused significant crustal compression and shear zone reactivation in Carajás, whereas Rio Maria largely retained its original architecture (Pinheiro and Holdsworth, 2000). The Sapucaia Subdomain, at their boundary, records this transition. It exhibits basement flattening, folding, intense shearing, and transposition of deformation, with migmatization, metamorphism, and mylonitization (Leite et al., 2004; Nascimento et al., 2024). While previously considered distinct, isotopic data suggest Rio Maria and Carajás share a common evolution with heterogeneous deformation (Nascimento et al., 2024; This study). Before 2.95 Ga, sagduction and drip tectonics formed dome-and-keel structures, with TTG magmas intruding greenstone sequences (Fig. 10a). The 2.95 – 2.92 Ga collision induced crustal thickening, faulting, and TTG emplacement (Fig. 10b). Between 2.89 – 2.84 Ga, intensified subduction led to granulite exhumation and sanukitoid intrusion. Tectonic reactivation facilitated syntectonic granite emplacement, marking a shift from vertical to horizontal tectonics and stabilizing the continental crust (Fig. 10c). These events reflect global Archean tectonics, demonstrating lithospheric reworking via subduction and collision, shaping the complex history of the Sapucaia Subdomain and broader Carajás Province (Palin et al., 2020).

The genesis of sanukitoids in the Carajás Province is also discussed in this proposed model. As previously reported, Costa et al. (2020) proposed that sanukitoids formed under a vertical tectonic regime. However, this model lacks robust petrological, isotopic, and structural evidence to explain mantle metasomatism. The vertical tectonics may account for localized melting and moderate enrichment in large-ion lithophile elements (LILE), but it fails to fully explain the pronounced geochemical features of Archean sanukitoids, such as high Mg, Cr, and Ni contents and significant HFSE depletion. Conversely, subduction models provide a more plausible framework, with slab-derived fluids metasomatizing the mantle wedge, leading to enhanced LILE enrichment and arc-like geochemical signatures (Heilimo et al., 2013; Laurent et al., 2014). Isotopic data from this study also supports a subduction-related origin, indicating mantle-derived sources with slab input and crustal contamination. A possible process causing the partial melting of the mantle is the breakoff of the subducting slab (Silva et al., 2023). This mechanism could allow for variable input from high $\delta^{18}O$ reservoirs (altered upper oceanic crust, fluids, or sediments) and lower $\delta^{18}O$ reservoirs (lower oceanic crust, man-

tle), as well as asthenospheric upwelling causing mantle metasomatism and partial melting in the mantle wedge, as suggested in other Archean cratons worldwide (Whalen et al., 2004; Heilimo et al., 2013). An alternative mechanism could involve abrupt crustal delamination after the accretion of continental crust, as discussed by Whalen et al. (2004) and Heilimo et al. (2010). The temporal restriction of sanukitoids to the late Archean further aligns with a transition from vertical to horizontal tectonic processes, associated with terrane amalgamation and continental collision (Cawood et al., 2018; Palin et al., 2020; Silva et al., 2023).

8.3. Can sanukitoids be produced in a vertical tectonic regime?

The formation of sanukitoids within a vertical tectonic regime underscores the challenges involved of applying uniformitarian models to Archaean craton formation (Bédard, 2018; Cawood et al., 2018; Nebel et al., 2018). The role of mantle plumes or vertical tectonics (e.g., sagduction) in mantle metasomatism remains unclear. Could vertical tectonic models provide an alternative framework in which to interpret our observations? Sanukitoids are often encountered bordering dome-and-keel structures or associated with regional shear zones within Archean granite–greenstone terranes worldwide (Moyen et al., 2003). In the Sapucaia subdomain of the Carajás Province, the Água Limpa and Água Azul sanukitoid plutons are spatially associated with east–west sinistral transpressive shear zones, which border dome-and-keel structures (Gabriel and Oliveira, 2014; Nascimento et al., 2024). Some researchers have attributed the occurrence of sanukitoids and others calc-alkaline granitoids in a dome-and-keel setting to their formation related to vertical regime (Costa et al., 2020), however the structural setting fail to fully explain the distinct geochemical features of Archean sanukitoids. These include LILE (e.g., K, Ba, and Sr) enrichment, HFSE depletion (Nb-Ta-Ti anomalies), trace element ratios (low Nb/Th), and high Mg#, Cr, and Ni contents (Heilimo et al., 2013; Nascimento et al., 2024). Vertical tectonic regimes, if responsible for sanukitoid genesis, would produce low LILE enrichment (< 200 ppm) due to intracrustal recycling and partial melting, less pronounced HFSE depletion, and moderate Sr/Y and La/Yb ratios (Nascimento et al., 2024). These features would result from localized melting and assimilation of lower crustal material. Conversely, subduction setting provides a more plausible explanation for sanukitoids genesis, as they account for significant LILE enrichment through slab-derived fluids or melts metasomatizing the mantle wedge. Additionally, this regime explains HFSE depletion due to residual phases retention (e.g., rutile), elevated Sr/Y (> 2.0) and La/Yb (> 1.5) ratios indicative of garnet stability in the source, and arc-like geochemical signatures, such as high Ba/Th and Th/Nb ratios reflective of slab contributions (Heilimo et al., 2013; Silva et al., 2023).

Regarding isotopic characteristics, vertical tectonic regimes might produce sanukitoids with subchondritic isotopic values, including negative $\varepsilon_{Hf}(t)$ and $\varepsilon_{Nd}(t)$, short crustal residence times (older model ages > 3.0 Ga), elevated $\delta^{18}O$ values (> 6.5 ‰), and moderate μ ($^{238}U/^{204}Pb$ = 4 % – 6 %) values in K-feldspar, indicative of dominantly crustal sources with minimal mantle interaction (Halla, 2005; Valley et al., 2005). However, the findings of this study indicate that Archean sanukitoids predominantly exhibit suprachondritic isotopic values, including positive $\varepsilon_{Hf}(t)$ and $\varepsilon_{Nd}(t)$ with slightly negative components, short crustal residence times (< 3.0 Ga), mantle-like $\delta^{18}O$ values (5.0 ‰ ± 0.5 ‰) or slightly elevated $\delta^{18}O$ values in some samples (> 6.5 ‰), and high μ values (> 10) related to an enriched mantle source. These features underscore a dual geochemical origin, reflecting mantle-derived source with significant slab input and potential crustal contamination (Valley et al., 2005). Furthermore, vertical tectonic processes, characterized by localized heat, limited recycling scales, and shallow depths, are generally insufficient to generate the substantial mantle metasomatism and significant sanukitoid volumes observed (Nebel et al., 2018). The limited efficiency of vertical tectonics in facilitating mantle-crust interactions and mantle metasomatism, combined with their localized nature and lower thermal gradients, renders this model less favorable for explaining sanukitoid genesis. Additionally, the pure vertical mechanism cannot adequately account for the ascent of dense mafic and ultramafic rocks from lower crustal levels (Nebel et al., 2018).

9. Conclusions

(1) The Água Limpa suite sanukitoids exhibit zircon $\varepsilon_{Hf}(t)$ values between –3.31 and + 2.14, Hf model ages (T_{DM}^{C}) from 2.98 Ga to 3.28 Ga, Nd-T_{DM} ages spanning 2.91 Ga to 3.15 Ga, and $\delta^{18}O$ values ranging from 5.0 ‰ to 7.6 ‰. These isotopic signatures are compatible with magmas derived mainly from a juvenile mantle source that experienced crustal assimilation. Whole-rock $\varepsilon_{Nd}(t)$ values (–1.64 to +1.76) and high μ Pb compositions in K-feldspar further support a mantle origin modified by interaction with crustal materials.

(2) Geochemical modeling suggests the origin of these sanukitoids involved partial melting (~15 %) of a mantle source metasomatized by approximately 30 % slab-derived components. Residual assemblages include phases such as orthopyroxene, garnet, clinopyroxene, magnetite, and phlogopite — the latter indicating more pronounced crustal input in specific rock types.

(3) The ascent and emplacement of the studied sanukitoid magmas likely occurred in upper crustal levels, facilitated by pre-existing shear zones that enhanced interaction between ascending mantle-derived magmas and the continental crust.

(4) The petrogenesis of the Água Limpa suite is best explained by geodynamic settings involving lateral tectonic movement, particularly subduction of oceanic lithosphere followed by accretionary collision. This tectonic scenario allowed for rapid generation and emplacement of mantle- and crust-derived melts around 2.87 Ga, in agreement with models for sanukitoid formation elsewhere in the Carajás Province and other Archean terranes.

CRediT authorship contribution statement

Aline Costa do Nascimento: Writing – original draft, Methodology, Investigation, Formal analysis, Conceptualization. **Davis Carvalho de Oliveira:** Writing – review & editing, Supervision. **Esa Heilimo:** Writing – review & editing, Supervision. **Marco Antonio Galarza:** Methodology, Formal analysis. **Eleilson Oliveira Gabriel:** Methodology. **Martin Whitehouse:** Methodology. **Matti Kurhila:** Methodology. **Cláudio Nery Lamarão:** Validation.

Declaration of competing interest

The authors declare that they have no known competing financial interests or personal relationships that could have appeared to influence the work reported in this paper.

Acknowledgements

The authors warmly thank Kerstin Lindén (NordSIMS) for preparing the zircon mounts used in the oxygen studies, and Arto Peltola (University of Turku, UTU) for preparing the feldspar mounts for the Pb-Pb analysis. Thanks are also extended to Ermai Mäkilä (UTU) for providing SEM images, and to Gisele Marques

for technical support in the Microanalysis Laboratory (UFPA). We acknowledge the Materials Research Infrastructure (MARI) at the Department of Physics and Astronomy, University of Turku, for access to and support with the SEM facilities. Heejin Jeon and Xuan Liu are also thanked for their assistance during the analytical sessions at the NordSIMS and GTK (Espoo, Finland) laboratories, respectively. NordSIMS is supported through funding by the Swedish Museum of Natural History and the Swedish Research Council via infrastructure grant 2021-00276. This is NordSIMS publication number 807. This work received financial support from the Brazilian Council for Scientific and Technological Development (CNPq) through a PhD scholarship grant (140684/2021-2) and Productivity grants (311647/2019-7 and 312151/2023-3) and Research project (406227/2023-3). Additional funding was provided by the Coordination for the Improvement of Higher Education Personnel (CAPES) through an exchange program (PDSE-2024 grant: 88881.934051/2024-01). We are grateful to the editor, Federico Lucci, for their efficient handling of the editorial process, and to Armin Zeh and an anonymous reviewer for their valuable contributions.

Appendix A. Supplementary data

Supplementary data to this article can be found online at https://doi.org/10.1016/j.gsf.2025.102172.

References

Albaréde, F., 1995. Introduction to Geochemical Modeling. Cambridge University Press, Cambridge. https://doi.org/10.1017/CBO9780511622960.

Albert, C., Farina, F., Lana, C., Stevens, G., Storey, C., Gerdes, A., Dopico, C.M., 2016. Archean crustal evolution in the Southern S ~ao Francisco craton, Brazil: Constraints from U-Pb, Lu-Hf and O isotope analyses. Lithos 266-267, 64–86. https://doi.org/10.1016/j.lithos.2016.09.029.

Almeida, F.F.M., Hasui, Y., Brito Neves, B.B., Fuck, R.A., 1981. Brazilian structural provinces: an introduction. Earth Sci. Rev. 17, 1–29. https://doi.org/10.1016/0012-8252(81)90003-9.

Almeida, J.A.C., Dall'Agnol, R., Oliveira, M.A., Macambira, M.J.B., Pimentel, M.M., Rämö, O.T., Guimarães, F.V., Leite, A.A.S., 2011. Zircon geochronology, geochemistry and origin of the TTG suites of the Rio Maria granite–greenstone terrane: implications for the growth of the Archean crust of the Carajás Province, Brazil. Precambrian Res. 187, 201–221. https://doi.org/10.1016/j.precamres.2011.03.004.

Almeida, J.A.C., Dall'Agnol, R., Leite, A.A.S., 2013. Geochemistry and zircon geochronology of the Archean granite suites of the Rio Maria granite–greenstone terrane, Carajás Province, Brazil. J. South Am. Earth Sci. 42, 103–126. https://doi.org/10.1016/j.jsames.2012.10.008.

Andersen, T., Andersson, U.B., Graham, S., Åberg, G., Simonsen, S.L., 2009. Granitic magmatism by melting of juvenile continental crust: new constraints on the source of Paleoproterozoic granitoids in Fennoscandia from Hf isotopes in zircon. J. Geol. Soc. 166, 233–248. https://doi.org/10.1144/0016-76492007-166.

Armistead, S., Eglington, B.M., Pehrsson, S.J., 2023. PbIso: an R package and web app for calculation and plotting Pb isotope data. Can. J. Earth Sci. 61 (1), 1–15. https://doi.org/10.1139/cjes-2023-0029.

Assis, C.R.F., Moura, C.A.V., Milhomem Neto, J.M., Gorayeb, P.S.S., Dias, A.N.C., 2021. Zircon U-Pb geochronology and Lu-Hf isotope systematics of the Araguaia Belt basement Rocks: Evidence of links with the southeastern Amazonian Craton, Brazil. Precambrian Res. 356, 106090. https://doi.org/10.1016/j.precamres.2020.106090.

Bauer, A.M., Fisher, C.M., Vervoort, J.D., Bowring, S.A., 2017. Coupled zircon Lu–Hf and U–Pb isotopic analyses of the oldest terrestrial crust, the >4.03 Ga Acasta Gneiss Complex. Earth Planet. Sci. Lett. 458, 37–48. https://doi.org/10.1016/j.epsl.2016.10.036.

Bédard, J.H., 2018. Stagnant lids and mantle overturns: Implications for Archaean tectonics, magma genesis, crustal growth, mantle evolution, and the start of plate tectonics. Geosci. Front. 9, 19–49. https://doi.org/10.1016/j.gsf.2017.01.005.

Belousova, E.A., Kostitsyn, Y.A., Griffin, W.L., Begg, G.C., O'Reilly, S.Y., Pearson, N.J., 2010. The growth of the continental crust: Constraints from zircon Hf-isotope data. Lithos 119 (3–4), 457–466. https://doi.org/10.1016/j.lithos.2010.07.024.

Ben Othman, D., Fourcade, S., Allégre, C.J., 1984. Recycling process in granite-granodiorite complex genesis: the Querigut case studied by Nd-Sr isotope systematic. Earth Planet. Sci. Lett. 69, 290–300. https://doi.org/10.1016/0012-821X(84)90188-2.

Bouvier, A., Vervoort, J.D., Patchett, P.J., 2008. The Lu–Hf and Sm–Nd isotopic composition of CHUR: Constraints from unequilibrated chondrites and implications for the bulk composition of terrestrial planets. Earth Planet. Sci. Lett. 273, 48–57. https://doi.org/10.1016/j.epsl.2008.06.010.

Cawood, P.A., Hawkesworth, C.J., Pisarevsky, S.A., Dhuime, B., Capitanio, F.A., Nebel, O., 2018. Geological archive of the onset of plate tectonics. Phil. Trans. R. Soc. A 376, 20170405. https://doi.org/10.1098/rsta.2017.0405.

Chauvel, C., Lewin, E., Carpentier, M., Arndt, N.T., Marini, J.C., 2008. Role of recycled oceanic basalt and sediment in generating the Hf-Nd mantle-array. Nat. Geosci. 1, 64–67. https://doi.org/10.1038/ngeo.2007.51.

Choukroune, P., Ludden, J.N., Chardon, D., Calvert, A.J., Bouhallier, H., 1997. Archaean crustal growth and tectonic processes: a comparison of the Superior Province, Canadá and the Dharwar Craton, India. Geol. Soc. London. Spec. Publ. 121, 63–98. https://doi.org/10.1144/GSL.SP.1997.121.01.04.

Costa, F.G., Santos, P.A., Serafim, I.C.C.O., Costa, I.S.L., Roopnarain, S., 2020. From Mesoarchean drips to modern–style tectonics in the Carajás Province, Amazonian Craton. J. South Am. Earth Sci. 104, 102817. https://doi.org/10.1016/j.jsames.2020.102817.

Cordani, U.G., Sato, K., Teixeira, W., Tassinari, C.C.G., Basei, M.A.S., 2000. Crustal evolution of the South American platform. In: Cordani, U.G., Milani, E.J., Thomaz Filho, A., Campos, D.A. (Eds.), Tectonic Evolution of South America. 31st International Geological Congress. Brazil Federal Mines Department, pp. 19–40. https://doi.org/10.18814/epiiugs/1999/v22i3/003.

Dall'Agnol, R., Oliveira, D.C., 2007. Oxidized, magnetite-series, rapakivi-type granites of Carajás, Brazil: implications for classification and petrogenesis of A-type granites. Lithos 93, 215–233. https://doi.org/10.1016/j.lithos.2006.03.065.

DePaolo, D.J., Wasserburg, G.J., 1976. Nd isotopic variations and petrogenetic models. Geophys. Res. Lett. 3, 249–252. https://doi.org/10.1029/GL003i005p00249.

Davis, D.W., Amelin, Y., Nowell, G.M., Parrish, R.R., 2005. Hf isotopes in zircon from the western Superior province, Canada: Implications for Archean crustal development andevolution of the depleted mantle reservoir. Precambrian Res. 140, 132–156. https://doi.org/10.1016/j.precamres.2005.07.005.

DePaolo, D.J., 1981. Trace element and isotopic effects of combined wall rock assimilation and fractional crystallization. Earth Planet. Sci. Lett. 53 (2), 189–202. https://doi.org/10.1016/0012-821X(81)90153-9.

Ersoy, Y., Helvaci, C., 2010. FC–AFC–FCA and mixing modeler: a Microsoft Excel spreadsheet program for modeling geochemical differentiation of magma by crystal fractionation, crustal assimilation and mixing. Comput. Geosci. 36 (3), 383–390. https://doi.org/10.1016/j.cageo.2009.06.007.

Diwu, C., Sun, Y., Si, B., Yan, M., 2024. Archean continental crustal growth and reworking of the North China Craton: Constraints from zircon U–Pb age and Hf isotopic composition. Earth-Sci. Rev. 248, 104624. https://doi.org/10.1016/j.earscirev.2023.104624.

Eiler, J.M., 2001. Oxygen isotope variations of basaltic lavas and upper mantle rocks. Rev. Mineral. Geochem. 43, 319–364. https://doi.org/10.2138/gsrmg.43.1.319.

Dall'Agnol, R., Oliveira, D.C., Lamarão, C.N., 2013. Geology of the transition subdomain of the Carajás Domain – implications for the Archean evolution of the Carajás Province – Pará. Abstract published at the 13th Symposium on Geology of the Amazon, 22–26 September, Belém, Pará, Brazil (in Portuguese with English abstract).

Feio, G.R.L., Dall'Agnol, R., Dantas, E.L., Macambira, M.J.B., Santos, J.O.S., Althoff, F.J., Soares, J.E.B., 2013. Archean granitoid magmatism in the Canaã dos Carajás area: implications for crustal evolution of the Carajás Province, Amazonian Craton, Brazil. Precambrian Res. 227, 157–185. https://doi.org/10.1016/j.precamres.2012.04.007.

Felix, W.Q., Oliveira, D.C., Silva, L.R., Silva, F.F., 2020. Charnockites from Carajás Province, SE Amazonian Craton (Brazil): petrogenetic constraints and intensive crystallization parameters. J. South Am. Earth Sci. 101, 102598. https://doi.org/10.1016/j.jsames.2020.102598.

Fisher, C.M., Vervoort, J.D., 2018. Using the magmatic record to constrain the growth of continental crust—The Eoarchean zircon Hf record of Greenland. Earth Planet. Sci. Lett. 488, 79–91. https://doi.org/10.1016/j.epsl.2018.01.031.

Frost, B.R., Barnes, C.G., Collins, W.J., Arculus, R.J., Ellis, D.J., Frost, C.D., 2001. A geochemical classification for granitic rocks. J. Petrol. 42 (11), 2033–2048. https://doi.org/10.1093/petrology/42.11.2033.

Fu, J.H., Liu, S.W., Cawood, P.A., Wang, M.J., Hu, F.Y., Sun, G.Z., Gao, L., Hu, Y.L., 2018. Neoarchean magmatic arc in the Western Liaoning Province, northern North China Craton: Geochemical and isotopic constraints from sanukitoids and associated granitoids. Lithos 322, 296–311. https://doi.org/10.1016/j.lithos.2018.10.024.

Gabriel, E.O., Oliveira, D.C., 2014. Geology, petrography and geochemistry of the Archean high-magnesium granitoids from the Água Azul do Norte region, southern portion of the Carajás Domain, Pará. Boletim Do Museu Paraense Emílio Goeldi Ciências Naturais 9, 533–564. https://doi.org/10.46357/bcnaturais.v9i3.509 (in Portuguese with English abstract)..

Gabriel, E.O., Oliveira, D.C., Galarza, M.A., 2010. Geology, petrography and geochronology of granitoids of the Xingu complex in the northeastern region of Água Azul do Norte – PA, Carajás Mineral Province. In: SBG Abstracts, 45th Brazilian Congress of Geology, Belém (in Portuguese).

Griffin, W.L., Pearson, N.J., Belousova, E.A., Saeed, A., 2006. Comment: Hf-isotope heterogeneity in zircon 91500. Chem. Geol. 233, 258–363. https://doi.org/10.1016/j.chemgeo.2006.03.007.

Griffin, W.L., Wang, X., Jackson, S.E., Pearson, N.J., O'Reilly, S., Xu, X., Zhou., X., 2002. Zircon chemistry and magma mixing, SE China: In-situ analysis of Hf isotopes, Tonglu and Pingtan igneous complexes. Lithos 61(3-4), 237–269. https://doi.org/10.1016/S0024-4937(02)00082-8.

Halla, J., 2005. Late Archean high-Mg granitoids (sanukitoids) in the southern Karelian domain, eastern Finland. Lithos 79, 161–178. https://doi.org/10.1016/j.lithos.2004.05.007.

Halla, J., 2018. Pb isotopes – a multi-function tool for assessing tectonothermal events and crust–mantle recycling at late Archaean convergent margins. Lithos 320–321, 207–221. https://doi.org/10.1016/j.lithos.2018.08.031.

Heilimo, E., Halla, J., Holttä, P., 2010. Discrimination and origin of the sanukitoid series: geochemical constraints from the Neoarchean western Karelian Province (Finland). Lithos 115, 27–39. https://doi.org/10.1016/j.lithos.2009.11.001.

Heilimo, E., Halla, J., Andersen, T., Huhma, H., 2013. Neoarchean crustal recycling and mantle metasomatism: Hf–Nd–Pb–O isotope evidence from sanukitoids of the Fennoscandian shield. Precambrian Res. 228, 250–266. https://doi.org/10.1016/j.precamres.2012.01.015.

Heinonen, A., Andersen, T., Rämö, O.T., Whitehouse, M., 2015. The source of Proterozoic anorthosite and rapakivi granite magmatism: evidence from combined in situ Hf–O isotopes of zircon in the Ahvenisto complex, southeastern Finland. J. Geol. Soc. 172 (1), 103–112. https://doi.org/10.1144/jgs2014-013.

Hermann, J., Spandler, C., Hack, A., Korsakov, A., 2006. Aqueous fluids and hydrous melts in high-pressure and ultrahigh-pressure rocks: Implications for element transfer in subduction zones. Lithos 92 (3–4), 399–417. https://doi.org/10.1016/j.lithos.2006.03.054.

Hu, Y.L., Liu, S.W., Gao, L., Sun, G.Z., Guo, R.R., Fu, J.H., Wang, M.J., Hu, F.Y., 2019. Diverse middle Neoarchean granitoids and the delamination of thickened crust in the Western Shandong Terrane, North China Craton. Lithos 348–349, 105178. https://doi.org/10.1016/j.lithos.2019.105178.

Janoušek, V., Moyen, J.-F., Martin, H., Erban, V., Farrow, C., 2015. Geochemical Modelling of Igneous Processes – Principles and Recipes in R Language. Bringing the Power of R to a Geochemical Community. Springer, 1st Ed. https://doi.org/10.1007/978-3-662-46792-3.

Jiang, N., Guo, J.H., Fan, W.B., Hu, J., Zong, K.Q., Zhang, S.Q., 2016. Archean TTGs and sanukitoids from the Jiaobei terrain, North China Craton: Insights into crustal growth and mantle metasomatism. Precambrian Res. 281, 656–672. https://doi.org/10.1016/j.precamres.2016.06.019.

Johnson, M.C., Plank, T., 1999. Dehydration and melting experiments constrain the fate of subducted sediments. Geochem. Geophys. Geosyst. 1 (12), 1007. https://doi.org/10.1029/1999GC000014.

Johnson, T.E., Brown, M., Kaus, B.J.P., VanTongeren, J.A., 2014. Delamination and recycling of Archaean crust caused by gravitational instabilities. Nat. Geosci. 7 (1), 47–52. https://doi.org/10.1038/ngeo2019.

Kessel, R., Schmidt, M.W., Ulmer, P., Pettke, T., 2005. Trace element signature of subduction-zone fluids, melts and supercritical liquids at 120–180 km depth. Nature 437, 724–727. https://doi.org/10.1038/nature03971.

Kent, A.J.R., 2008. Lead isotope homogeneity of NIST SRM 610 and 612 glass reference materials: Constraints from laser ablation multicollector ICP-MS (LA-MC-ICP-MS) analysis. Geostand. Geoanal. Res. 32 (2), 129–147. https://doi.org/10.1111/j.1751-908X.2008.00872.x.

Kemp, A.I., Vervoort, J.D., Petersson, A., Smithies, R.H., Lu, Y., 2023. A linked evolution for granite-greenstone terranes of the Pilbara Craton from Nd and Hf isotopes, with implications for Archean continental growth. Earth Planet. Sci. Lett. 601, 117895. https://doi.org/10.1016/j.epsl.2022.117895.

Kemp, A.I.S., Wilde, S.A., Hawkeswoth, C.J., Coath, C.D., Nemchin, A., Pidgeon, R.T., Vervoort, J.D., DuFrane, S.A., 2010. Hadean crustal evolution revisited: New constraints from Pb–Hf isotope systematics of the Jack Hills zircons. Earth Planet. Sci. Lett. 296, 45–56. https://doi.org/10.1016/j.epsl.2010.04.043.

Kuribara, Y., Tsunogae, T., Santosh, M., Takamura, Y., Costa, A.G., Rosière, C.A., 2019. Eoarchean to Neoproterozoic crustal evolution of the Mantiqueira and the Juiz de Fora Complexes, SE Brazil: Petrology, geochemistry, zircon U-Pb geochronology and Lu-Hf isotopes. Precambrian Res. 323, 82–101. https://doi.org/10.1016/j.precamres.2019.01.008.

Laurent, O., Martin, H., Moyen, J.F., Doucelance, R., 2014. The diversity and evolution of late-Archean granitoids: evidence for the onset of "modern-style" plate tectonics between 3.0 and 2.5 Ga. Lithos 205, 208–235. https://doi.org/10.1016/j.lithos.2014.06.012.

Laurent, O., Björnsen, J., Wotzlaw, J.-F., Bretscher, S., Pimenta Silva, M., Moyen, J.-F., Ulmer, P., Bachmann, O., 2020. Earth's earliest granitoidsare crystal-rich magma reservoirs tapped by siliciceruptions. Nat. Geosci. 13, 163–169. https://doi.org/10.1038/s41561-019-0520-6.

Leite, A.A.S., 2001. Geochemistry, petrogenesis and structural evolution of the Archean granitoids of the Xinguara region, SE of the Amazonian Craton. PhD thesis, Federal University of Pará (in Portuguese).

Leite, A.A.S., Dall'Agnol, R., Macambira, M.J.B., Althoff, F.J., 2004. Geology and geochronology of the Archean granitoids of the Xinguara region (PA) and their implications for the evolution of the Rio Maria Granite–Greenstone Terrain. Brazil. J. Geosci. 34, 447–458 (in Portuguese with English abstract). https://doi.org/10.25249/0375-7536.2004344447458.

Leite-Santos, P.J.S., Oliveira, D.C., 2016. Geology, petrography and geochemistry of the Archean leucogranitic associations of the Nova Canadá area, Carajás Province. USP Geology Journal 16(2), 37–66 (in Portuguese with English abstract). https://doi.org/10.11606//issn.2316-9095.v16i2p37-66.

Li, X., Tang, G., Gong. B., Yang., Y., Hou, K., Hu, Z., Li, Q., Liu, Y., Li, W., 2013. Qinghu zircon: A working reference for microbeam analysis of U-Pb age and Hf and O isotopes. Chin. Sci. Bull. 58(36), 4647–4654. https://doi.org/10.1007/s11434-013-5932-x.

Laurent, O., Zeh, A., 2015. A linear Hf isotope-age array despite different granitoid sources and complex Archean geodynamics: Example from the Pietersburg block (South Africa). Earth Planet. Sci. Lett. 430, 326–338. https://doi.org/10.1016/j.epsl.2015.08.028.

Li, S.Z., Suo, Y.H., Li, X.Y., Liu, B., 2018. Microplate tectonics: new insights from micro-blocks in the global oceans, continental margins and deep mantle. Earth Sci. Rev. 185, 1029–1064. https://doi.org/10.1016/j.earscirev.2018.09.005.

Lugmair, G.W., Marti, K., 1978. Lunar initial $^{143}Nd/^{144}Nd$: Differential evolution of the lunar crust and mantle. Earth Planet. Sci. Lett. 39 (3), 349–357. https://doi.org/10.1016/0012-821X(78)90021-3.

Marangoanha, B., Oliveira, D.C., Galarza, M.A., Marques, G.T., 2020. Crustal anatexis and mantle-derived magmas forming Neoarchean A-type granitoids in Carajás Province, northern Brazil: petrological evidence and tectonic control. Precambrian Res. 338, 105585. https://doi.org/10.1016/j.precamres.2019.105585.

Martin, H., Moyen, J.F., Rapp, R.P., 2009. The sanukitoid series: magmatism at the Archaean-Proterozoic transition. Earth Environ. Sci. Trans. R. Soc. Edinb. 100, 15–33. https://doi.org/10.1017/S1755691009016120.

Martin, H., Smithies, R.H., Rapp, R., Moyen, J.F., Champion, D., 2005. An overview of adakite, tonalite–trondhjemite–granodiorite (TTG), and sanukitoid: relationships and some implications for crustal evolution. Lithos 79, 1–24. https://doi.org/10.1016/j.lithos.2004.04.048.

McDonough, W.F., 2014. Compositional models for the Earth's core. In: Carlson, R. W. (Ed.), Treatise on Geochemistry: The Mantle. Elsevier, vol. 2, pp. 547–568. https://doi.org/10.1016/B0-08-043751-6/02015-6.

Milhomem Neto, J.M., Lafon, J.M., 2019. Zircon U-Pb and Lu-Hf isotope constraints on Archean crustal evolution in Southeastern Guyana Shield. Geosci. Front. 10, 1477–1506. https://doi.org/10.1016/j.gsf.2018.09.012.

Mole, D.R., Kirkland, C.L., Fiorentini, M.L., Barnes, S.J., Cassidy, K.F., Isaac, C., Belousova, E.A., Hartnady, M., Thebaud, N., 2019. Time-space evolution of an Archean craton: a Hf-isotope window into continent formation. Earth Sci. Rev. 196, 102831. https://doi.org/10.1016/j.earscirev.2019.04.003.

Morel, M.L.A., Nebel, O., Nebel-Jacobsen, Y.J., Miller, J.S., Vroon, P.Z., 2008. Hafnium isotope characterization of the GJ-1 zircon reference material by solution and laser- ablation MC-ICPMS. Chem. Geol. 255, 231–235. https://doi.org/10.1016/j.chemgeo.2008.06.040.

Moyen, J.F., Martin, H., Jayananda, M., Auvray, B., 2003. Late Archaean granites: a typology based on the Dharwar Craton (India). Precambrian Res. 127, 103–123. https://doi.org/10.1016/S0301-9268(03)00183-9.

Moyen, J.F., Martin, H., Jayananda, M., 2001. Multi-element geochemical modelling of crust–mantle interactions during late-Archaean crustal growth: the Closepet granite (South India). Precambrian Res. 112, 87–105. https://doi.org/10.1016/S0301-9268(01)00171-1.

Moyen, J.F., McCoy-West, A.J., Bruand, E., Millet, M.A., Nebel, O., Cawood, P.A., Saji, N., Ladwig, A., Klaver, M., Elburg, M., 2024. Felsic crust development in the Kaapvaal Craton, South Africa: A reference sample collection to investigate a billion years of geological history. Earth-Sci. Rev. 250, 104680. https://doi.org/10.1016/j.earscirev.2024.104680.

Mulder, J.A., Nevel, O., Gardiner, N.J., Cawood, P.A., Wainwright, A.N., Ivanic, T.J., 2021. Crustal rejuvenation stabilised Earth's first cratons. Nat. Commun. 12, 3535. https://doi.org/10.1038/s41467-021-23805-6.

Nascimento, A.C., Oliveira, D.C., Gabriel, E.O., Leite-Santos, P.J., 2024. Geology, geochemistry and zircon SHRIMP U–Pb geochronology of Mesoarchean high-Mg granitoids: constraints on petrogenesis, emplacement timing and deformation of the Água Limpa suite in the Carajás Province, SE Amazonian Craton. J. Geol. Soc. 182, 1–20. https://doi.org/10.1144/jgs2024-098.

Nascimento, A.C., de Oliveira, D.C., Gabriel, E.O., Marangoanha, B., Silva, L.R., Aleixo, E.C., 2023. Mineral chemistry of the Água Limpa suite: insights into petrological constraints and magma ascent rate of Mesoarchean sanukitoids from the Sapucaia terrane (Carajás Province, southeastern Amazonian Craton, Brazil). J. South Am. Earth Sci. 132, 104683. https://doi.org/10.1016/j.jsames.2023.104683.

Nasdala, L., Hofmeister, W., Norberg, N., Mattinson, J.M., Corfu, F., Dörr, W., Kamo, S. L., Kennedy, A.K., Kronz, A., Reiners, P.W., Frei, D., Kosler, J., Wan, J., Götze, J., Häger, T., Kröner, A., Valley, J.W., 2008. Zircon M257 - a homogeneous natural reference material for the ion microprobe U-Pb analysis of zircon. Geostand. Geoanal. Res. 32 (3), 247–265. https://doi.org/10.1111/j.1751-908X.2008.00914.x.

Nebel, O., Capitanio, F.A., Moyen, J.-F., Weinberg, R.F., Clos, F., Nebel-Jacobsen, Y.J., Cawood, P.A., 2018. When crust comes of age: on the chemical evolution of Archaean, felsic continental crust by crustal drip tectonics. Phil. Trans. R. Soc. A 376, 20180103. https://doi.org/10.1098/rsta.2018.0103.

Oliveira, M.A., Dall'Agnol, R., Almeida, J.A.C., 2011. Petrology of the Mesoarchean Rio Maria suite and the discrimination of sanukitoid series. Lithos 127, 192–209. https://doi.org/10.1016/j.lithos.2011.08.017.

Oliveira, M.A., Dall'Agnol, R., Scaillet, B., 2010. Petrological constraints on crystallization conditions of Mesoarchean sanukitoid rocks, southeastern Amazonian Craton, Brazil. J. Petrol. 51(10), 2121–2148. https://doi.org/10.1093/petrology/egq051.

Oliveira, E.C., Lafon, J.M., Gioia, S.M.C.L., Pimentel, M.M., 2008. Sm-Nd dating on whole rock and garnet from the granulite facies metamorphism in the Tartarugal Grande region, central Amapá. Brazil. J. Geosci. 38, 114–127. https://doi.org/10.25249/0375-7536.2008381114127.

Oliveira, D.C., Silva, L.R., Nascimento, A.C., Marangoanha, B., Gabriel, E.O., Leite-Santos, P.J., Machado, J.R.M., Felix, W.Q., Silva-Silva, L.C., Santos, R.F., 2023. Lithostratigraphic review with implications for tectonic compartmentalization of the Carajás Mineral Province, southeastern Amazonian Craton. In: Abstracts proceedings of the 17th Symposium on Geology of the Amazon, Brazilian Geological Society, Santarém, 1, 434–441 (in Portuguese).

Palin, R.M., Santosh, M., Cao, W., Li, S., Hernández-Uribe, D., Parsons, A., 2020. Secular change and the onset of plate tectonics on Earth. Earth Sci. Rev. 207, 103172. https://doi.org/10.1016/j.earscirev.2020.103172.

Plank, T., Langmuir, C.H., 1998. The chemical composition of subducting sediment and its conseqiences for the crust and mantle. Chem. Geol. 145, 325–394. https://doi.org/10.1016/S0009-2541(97)00150-2.

Pinheiro, R.V.L., Holdsworth, R.E., 2000. Tectono-stratigraphic evolution of the Carajás and Cinzento strike-slip systems, Itacaiúnas Belt, at the eastern edge of the amazonian Craton – Pará. Brazil. J. Geosci. 30, 597–606. https://doi.org/10.25249/0375-7536.2000304597606 (in Portuguese).

Polat, A., Wang, L., Appel, P.W.U., 2015. A review of structural patterns and melting processes in the Archean craton of West Greenland: evidence for crustal growth at convergent plate margins as opposed to non-uniformitarian models. Tectonophysics 662, 67–94. https://doi.org/10.1016/j.tecto.2015.04.006.

Rapp, R.P., Norman, M.D., Laporte, D., Yaxley, G.M., Martin, H., Foley, S.F., 2010. Continent formation in the Archean and chemical evolution of the cratonic lithosphere: melt–rock reaction experiments at 3–4 GPa and petrogenesis of Archean Mg-diorites (sanukitoids). J. Petrol. 51, 1237–1266. https://doi.org/10.1093/petrology/egq017.

Santos, J.O.S., 2003. Geotectonics of the Guiana and Central Brazil Shields. In: Bizzi, L.A., Schobbenhaus, C., Vidotti, R.M.M., Gonçalves, J.H. (Eds.), Geology, Tectonics, and Mineral Resources of Brazil: Text, Maps, and GIS. CPRM – Geological Survey of Brazil, pp. 169–226 (in Portuguese).

Santos, M.S., Oliveira, D.C., Gabriel, E.O., 2018. TTG granitoids from Água Azul do Norte (PA): tectonic implications for the Carajás Province. USP Geol. J. 18, 119–148. https://doi.org/10.11606/issn.2316-9095.v18-126992 (in Portuguese)..

Ravindran, A., Mezger, K., Balakrishnan, S., Berndt, J., Ranjan, S., Upadhyay, D., 2023. Formation of Paleo- to Meso-Archean continental crust in the western Dharwar Craton, India: Constraints from U–Pb zircon ages and Hf-Pb-Sr isotopes of granitoids and sedimentary rocks. Chem. Geol. 615, 121196. https://doi.org/10.1016/j.chemgeo.2022.121196.

Santos, M.N.S., Oliveira, D.C., 2016. Rio Maria granodiorite and associated rocks of Ourilândia do Norte – Carajás Province: petrography, geochemistry and implications for sanukitoid petrogenesis. J. South Am. Earth Sci. 72, 279–301. https://doi.org/10.1016/j.jsames.2016.09.002.

Scherer, E., Münker, C., Mezger, K., 2001. Calibration of the lutetium-hafnium clock. Science 293, 683–687. https://doi.org/10.1126/science.1061372.

Schneider, K.P., Hoffmann, J.E., Boyet, M., Münker, C., Kröner, A., 2018. Coexistence of enriched and modern-like ^{142}Nd signatures in Archean igneous rocks of the eastern Kaapvaal Craton, southern Africa. Earth Planet. Sci. Lett. 487, 54–66. https://doi.org/10.1016/j.epsl.2018.01.022.

Silva, F.F., Oliveira, D.C., Dall'Agnol, R., Silva, L.R., Cunha, I.V., 2021. Lithological and structural controls on the emplacement of a Neoarchean plutonic complex in the Carajás province, southeastern Amazonian craton (Brazil). J. S. Am. Earth. Sci. 102, 102696. https://doi.org/10.1016/j.jsames.2020.102696.

Silva, L.R., Oliveira, D.C., Galarza, M.A., Nascimento, A.C., Marangoanha, B., Marques, G.T., 2023. Zircon U–Pb–Hf isotope and geochemical constraints on the petrogenesis and tectonic setting of Mesoarchean granitoids from the Carajás Province, amazonian Craton, Brazil. Precambrian Res. 398, 107204. https://doi.org/10.1016/j.precamres.2023.107204.

Silva, F.F., Oliveira, D.C., Dall'Agnol, R., Silva, L.R., Cunha, I.V., 2020. Lithological and structural controls on the emplacement of a Neoarchean plutonic complex in the Carajás province, southeastern Amazonian craton (Brazil). J. South Am. Earth Sci. 102, 102696. https://doi.org/10.1016/j.jsames.2020.102696.

Smithies, R.H., Champion, D.C., 2000. The Archean high-Mg diorite suite: links to tonalite–trondhjemite–granodiorite magmatism and implications for early Archean crustal growth. J. Petrol. 41, 1653–1671. https://doi.org/10.1093/petrology/41.12.1653.

Smithies, R.H., Lu, Y.J., Kirkland, C.L., Johnson, T.E., Mole, D.R., Champion, D.C., Martin, L., Jeon, H., Wingate, M.T.D., Johnson, S.P., 2021. Oxygen isotopes trace the origins of Earth's earliest continental crust. Nature 592 (7852), 70–75. https://doi.org/10.1038/s41586-021-03337-1.

Song, D., Xiao, W., Han, C., Tian, Z., Wang, Z., 2013. Provenance of metasedimentary rocks from the Beishan orogenic collage, southern Altaids: constraints from detrital zircon U-Pb and Hf isotopic data. Gondwana Res. 24, 1127–1151. https://doi.org/10.1016/j.gr.2013.02.002.

Sousa, S.D., Oliveira, D.C., Gabriel, E.O., Macambira, M.J.B., 2010. Geology, petrography, and geochronology of the granitoid rocks of the Xingu complex in the eastern portion of the city of Água Azul do Norte (PA) – Carajás Mineral Province. In: Abstracts of the 45th Brazilian Congress of Geology, Belém (in Portuguese).

Stacey, J.S., Kramers, J.D., 1975. Approximation of terrestrial lead isotope evolution by a two-stage model. Earth Planet. Sci. Lett. 26, 207–221. https://doi.org/10.1016/0012-821X(75)90088-6.

Stern, A.L., Hanson, G., 1991. Archean high-Mg granodiorite: a derivate of light rare earth element-enriched monzodiorite of mantle origin. J. Petrol. 32, 201–238. https://doi.org/10.1093/petrology/32.1.201.

Stevenson, R., Henry, P., Gariépy, C., 1999. Assimilation–fractional crystallization origin of Archaean sanukitoid suites: Western Superior Province, Canada. Precambrian Res. 96, 83–99. https://doi.org/10.1016/S0301-9268(99)00009-1.

Sun, G.Z., Liu, S.W., Gao, L., Hu, Y.L., Guo, R.R., Fu, J.H., Wang, M.J., Ma, C.C., Hu, F.Y., 2019. Neoarchean sanukitoids and associated rocks from the Tengzhou-Pingyi intrusive complex, North China Craton: Insights into petrogenesis and crust-mantle interactions. Gondwana Res. 68, 50–68. https://doi.org/10.1016/j.gr.2018.11.005.

Sun, G.Z., Liu, S.W., Wang, M.J., Bao, H., Teng, G.X., 2020. Complex Neoarchean mantle metasomatism: evidence from sanukitoid diorites-monzodiorites-granodiorites in the northeastern North China Craton. Precambrian Res. 342, 105692. https://doi.org/10.1016/j.precamres.2020.105692.

Sun, G.Z., Hu, Y.L., Liu, S.W., Li, S.Z., Fu, J.H., Gao, L., 2023. Featured Neoarchean granitoid association in the central North China Craton: an indicator of warm plate subduction. Geol. Soc. Am. Bull. 135 (1–2), 295–309. https://doi.org/10.1130/B36410.1.

Sun, G.Z., Liu, S.W., Li, S.Z., Kusky, T.M., Hu, F.Y., Bao, H., Gao, L., Hu, Y.L., Yu, S.Y., Dai, L.M., Wang, L.T., Wang, X., 2025. Neoarchean orogenic belt evolution in the northeast North China Craton: Implications for the reconstruction of early Earth's microplates. Precambrian Res. 417, 107659. https://doi.org/10.1016/j.precamres.2024.107659.

Tassinari, C.C.G., Macambira, M.J.B., 2004. Tectonic evolution of the Amazonian Craton. In: Mantesso Neto, V., Bartorelli, A., Carneiro, C.D.R., Bley de Brito-Neves, B.B. (Eds.), Geology of the South American Continent: Evolution of The Work of F.F.M. de Almeida. BECA, 471–486 (in Portuguese).

Terentiev, R.A., Santosh, M., 2018. High magnesian granitoids in the Precambrian continental crust: implication for the continuum between ferro-potassic and magnesio-potassic rock suites. Lithos 314–315, 669–682. https://doi.org/10.1016/j.lithos.2018.07.002.

Valley, J.W., Lackey, J.S., Cavosie, A.J., Clechenko, C.C., Spicuzza, M.J., Basei, M.A.S., Bindeman, I.N., Ferreira, V.P., Sial, A.N., King, E.M., Peck, W.H., Sinha, A.K., Wei, C.S., 2005. 4.4 billion years of crustal maturation: oxygen isotope ratios of magmatic zircon. Contrib. Mineral. Petrol. 150, 561–580. https://doi.org/10.1007/s00410-005-0025-8.

Valley, J.W., Kinny, P.D., Schulze, D.J., Spicuzza, M.J., 1998. Zircon megacrysts from kimberlite: Oxygen isotope variability among mantle melts. Contrib. Mineral. Petrol. 133, 1–11. https://doi.org/10.1007/s004100050432.

Vasquez, M.L., Rosa-Costa, L.T.R., 2008. Geology and mineral resources of Pará: explanatory text for the geological, tectonic, and mineral resource maps of the state of Pará. Belém: CPRM, p. 328, Scale 1:1,000,000. Geographic Information System (GIS), Brazil Geology Program (PGB) (in Portuguese).

Vervoort, J.D., Kemp, A.I.S., 2016. Clarifying the zircon Hf isotope record of crust-mantle evolution. Chem. Geol. 425, 65–75. https://doi.org/10.1016/j.chemgeo.2016.01.023.

Vervoort, J.D., Plank, T., Prytulak, J., 2011. Geochemistry of marine sediments of the world's major subduction zones. Geochim. Cosmochim. Acta 75 (20), 5903–5926. https://doi.org/10.1594/PANGAEA.782950.

Whalen, J.B., Percival, J.A., McNicoll, V.J., Longstaffe, F.J., 2004. Geochemical and isotopic (Nd-O) evidence bearing on the origin of late- to postorogenic high-K granitoids rocks in the Western Superior Province: implications for late Archean tectonomagmatic processes. Precambrian Res. 132, 303–326. https://doi.org/10.1016/j.precamres.2003.11.007.

Workman, R.K., Hart, S.R., 2005. Major and trace element composition of the depleted MORB mantle (DMM). Earth Planet. Sci. Lett. 231, 53–72. https://doi.org/10.1016/j.epsl.2004.12.005.

Zeh, A., Cabral, A.R., 2021. Combining detrital zircon shape and U–Pb–Hf isotope analyses for provenance studies – An example from the Aquiri region, Amazon Craton, Brazil. Precambrian Res 364, 106343. https://doi.org/10.1016/j.precamres.2021.106343.